



Elemental and isotopic tracing of mineral infillings from various microstructures of a fault system into fine-grained sediments: which interacting fluids?

Norbert Clauer, Isabelle Techer, Christophe Nussbaum

► To cite this version:

Norbert Clauer, Isabelle Techer, Christophe Nussbaum. Elemental and isotopic tracing of mineral infillings from various microstructures of a fault system into fine-grained sediments: which interacting fluids?. International Journal of Earth Sciences, 2022, 10.1007/s00531-021-02143-4 . hal-03556270

HAL Id: hal-03556270

<https://hal.science/hal-03556270>

Submitted on 18 Feb 2022

HAL is a multi-disciplinary open access archive for the deposit and dissemination of scientific research documents, whether they are published or not. The documents may come from teaching and research institutions in France or abroad, or from public or private research centers.

L'archive ouverte pluridisciplinaire **HAL**, est destinée au dépôt et à la diffusion de documents scientifiques de niveau recherche, publiés ou non, émanant des établissements d'enseignement et de recherche français ou étrangers, des laboratoires publics ou privés.

Elemental and isotopic tracing of mineral infillings from various microstructures of a fault system into fine-grained sediments: which interacting fluids?

Norbert Clauer¹ · Isabelle Techer² · Christophe Nussbaum³

Abstract

Elemental contents and Sr isotopic data of calcite and celestite infillings from various tectonic microstructures of the so-called “Main Fault” that occurs in the Opalinus Clay Formation (Switzerland) were used to elaborate on the geochemical impact of this structural system on the fine-grained host sediments. The chemical data of the leachates from vein, slickenside and gouge infillings are significantly different from those of leachates from diffuse calcite of the undeformed and of the highly deformed Opalinus Clay rock matrix called scaly clays. For instance, the fluids flowing within the microstructural veins and slickensides could not derive from pore waters of the host sediments, as the data show that the flowing waters diffused from veins into the matrix. The fluid/rock interactions in the gouges were also different from those in the veins and the slickensides, probably due to an additional pressure-solution impact in the former, complemented by a further local supply of organics from very close sediments. The infillings of the vein and slickenside micro-features and of some scaly clays that precipitated from bi-carbonated and/or sulfated flowing fluids yield an almost constant $^{87}\text{Sr}/^{86}\text{Sr}$ ratio of 0.70774 ± 0.00001 (2σ). This constrained Sr isotopic value points to a unique homogeneous external source for the tectonic-related fluids that were of probable marine origin, signing those of the early, but also of the late faulting event. Notably different from those seeping presently throughout the host rocks, the initial flowing fluids were apparently related to a late-Eocene marine invasion into the Delémont Basin that occurred during the contemporaneous rifting of the Rhine-Graben tectonic system. The flowing fluids induced by the late Main-Fault system obviously used, at least, some if not most of these earlier tectonic microstructures, as they yield the Sr isotopic signature of their infillings. The regional evolution includes then an initial Rhine-Graben tectonic episode with fluids resulting from a flooding of the deposited sediments and into the faults of the regional active Rhine-Graben rifting by contemporaneous seawater. These fluids precipitated precisely calcite and celestite infillings in the microstructures induced by the rifting that remained then unaffected until the renewed tectonic activation during the late Eocene in the Mont Terri and its fault system. This new tectonic–thermal episode created a new generation of microstructures during the thin-skinned deformation of the Jura Belt within and around the Main Fault, in addition to those from earlier Rhine-Graben event that already existed in the host rocks. Connections between the two generations of veins could be observed at the wall of a new gallery in the rock laboratory. The flowing fluids involved in this late belt event moved apparently along these newly created tectonic microstructures, as well as along older ones when accessible. This duality allowed the preservation of the same initial Sr isotopic signature by partial dissolution of the initial infillings that precipitated about 30 million years earlier in the initial drains of the Rhine-Graben fault system.

Keywords Tectonic veins, slickensides and gouges · Calcite and celestite infillings · Highly deformed scaly clays · Undeformed matrix · Elemental and Sr isotopic analyses · Mont Terri Main Fault

Introduction

Deformation bands of thin shear zones have often been described as incipient tectonic structures of compacted clay-rich sediments (e.g., Agar et al. 1989; Labaume et al. 1997; Dehandschutter et al. 2005; Ishii 2012). These shear

✉ Norbert Clauer
nclauer@unistra.fr

zones increase with strain, ultimately leading to the formation of clusters along fault planes (e.g., Rutter et al. 1986; Logan et al. 1992; Haines et al. 2013). As many structural and geochemical aspects are involved in the fabric of such features, their combination necessarily raises debates about, for instance, the origin and the impact of the accompanying fluids that expectedly interacted with the host minerals. The impact by such flowing fluids has not yet been addressed as often in faulting systems as it deserves: for instance, a very recent review by Steele-Macinnis and Manning (2020) about hydrothermal fluids did not dedicate any topic to low-metamorphic fluids related to tectonic environments. In claystones, the potential processes involved in mechanical interplays (e.g., Urai and Wong 1994; Ingram et al. 1997) induce particle reorientations and pore collapses in the fault volume (Morgenstern and Tchalenko 1967; Milliken and Reed 2010), as well as grain-size reduction (Bos and Spiers 2001; Mitra and Ismat 2001), grain-boundary sliding and mineral alterations (Warr and Cox 2001; Buatier et al. 2012). These are just a few of many processes that may explain microscopic features in shear zones. However, geochemical interpretations of such shear zones to explain the structures and processes involved remain limited, probably because of difficulties to collect pristine samples of fault systems with accurate descriptions (e.g., Schleicher et al. 2006; Sasseville et al. 2008). Indeed, successful separation and precise identification of very small crystals as structural infillings of tectonic micro-features remain challenging, especially when the microstructural veins or the gouges are of centimeter to millimeter sizes (e.g., Vrolijk and van der Pluijm 1999; Laurich et al. 2014). Also, samples of thin shear zones contain usually myriads of slickensides with smooth and shiny striated surfaces (*sensu* Passchier 2005) in combinations close to those often described in various rock types (Tjia 1964; Gay 1970; Means 1987; Petit and Laville 1987; Doblas 1998) that include claystones of concern here (Gray and Nickelsen 1989; Will and Wilson 1989; Saffer et al. 2012). The surfaces of such slickensides and the walls of their accompanying veins are often covered by tiny minerals that were deposited by migrating fluids, therefore containing useful chemical and isotopic information about these fluids.

In this context, the objectives of the present study are in a detailed chemical examination of the mineral infillings from microstructures induced by a thrust fault of the Swiss Jura, to complement the physical information of the features resulting from their mechanical impact on the host sediments. To do so, the interactions of fluids associated with the faulting are evaluated by a detailed chemical description of the infillings from microstructural features that were potentially used by the migrating fluids relative to the traces of pore fluids that diffused within the undeformed OPA matrix. In turn, the main concern includes a detailed chemical information to address concerns such as: (1) How does a structural system

impact the mineralogical and chemical characteristics of the host sediments? (2) How do flowing fluids migrate during an active tectonic period? (3) Along which tectonic (micro-) structures did the fluids flow? (4) What can be told about the origin(s) and nature(s) of the flowing fluids? (5) To which extent did the interactions interfere with the host minerals in the various microstructures in and around the fault? To answer appropriately these questions, the data generated here are combined with some of a previous publication (Clauer et al. 2017a) to widen the analytical database of the microstructural infillings, as well as of the diffuse calcite from main undeformed and slightly deformed host matrix.

The “Main Fault” has already been identified and described in the Opalinus Clay-rich sediments, especially in the Mont Terri rock laboratory (Switzerland) in relation with the evaluation of its storage potentials for nuclear waste (Fig. 1). Among the reasons for its study here are its pristine and easily accessible outcrops, especially in the galleries of the underground laboratory, which is not as common for fault systems. Of importance is also the fact that the fault itself is crosscut by numerous drill-holes (Bossart et al. 2017), both the outcrops and the cores providing high-quality samples that were easily identified.

The geological situation

The Opalinus Clay Formation (labeled as OPA hereafter) consists mostly of incompetent silty and sandy shales that were deposited between about 175 and 185 Ma. A structural feature of the fault was provided again recently by Nussbaum et al. (2017), together with its regional geological context. The fault is located in an anticline that developed at the junction between the frontal Jura thrust-and-fold belt and the Rhine–Bresse transfer zone, at the southern end of the Rhine-Graben (Ustaszewski et al. 2005; Ustaszewski and Schmid, 2007). Generally considered as a blind thrust, the Main Fault is now interpreted as a second-order fault that developed in the hanging wall of the Mont Terri anticline along the Rietheim Member at the top of the Staffelegg Formation (Fig. 1). Away from folded Mont Terri area that is of prime concern here, the OPA was subjected to a plain burial that reached temperatures of about 85 °C during the Cretaceous in northeastern Switzerland (Mazurek et al. 2006).

Easily accessible in the Mont Terri rock laboratory, the Main Fault crops out in a 0.8 by 3 m wide zone of a gallery with a reverse offset of about 50 m. It resulted from a highly heterogeneous strain that juxtaposes undeformed rocks next to highly strained equivalents (Fig. 2; Laurich et al. 2014; Jaeggi et al. 2017). While the porosity and microfabric of the tectonically undeformed OPA have been studied in detail (e.g., Holzer et al. 2006; Houben et al. 2013, 2014), little is still known about the mechanisms that induced the chemical

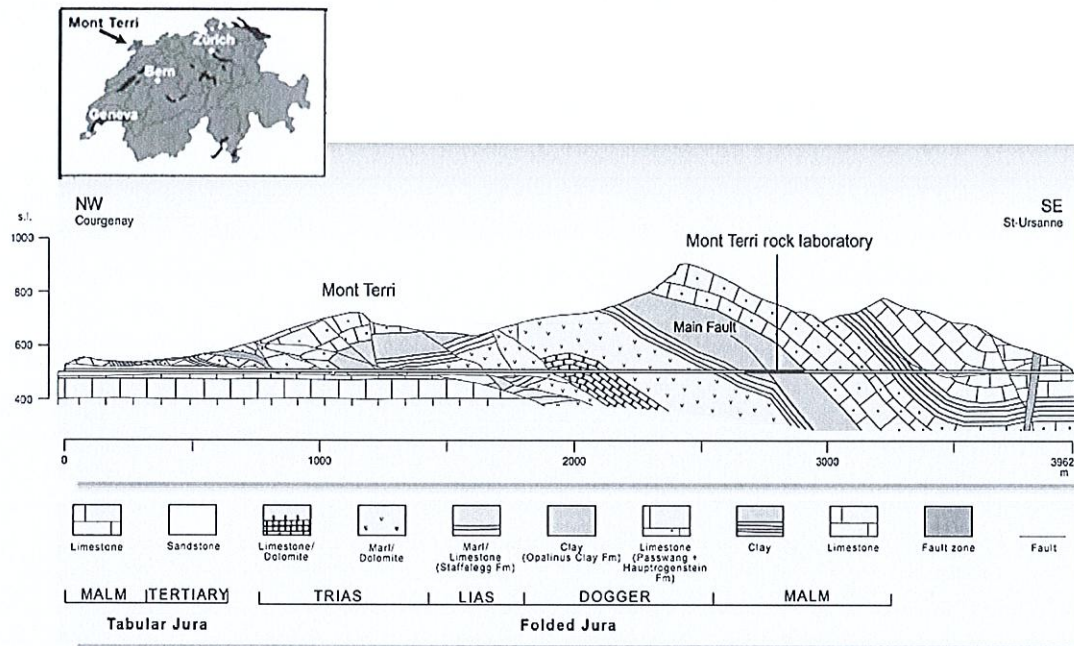


Fig.1 Regional cross section of the Mont Terri anticline and the Main Fault with the location of the rock laboratory (in red). The dotted red line sketches the fault plane in the Opalinus Clay (modified

from Nussbaum et al. 2017). The geographic location of the rock laboratory is given in the insert by the red dot in the northwestern corner of Switzerland

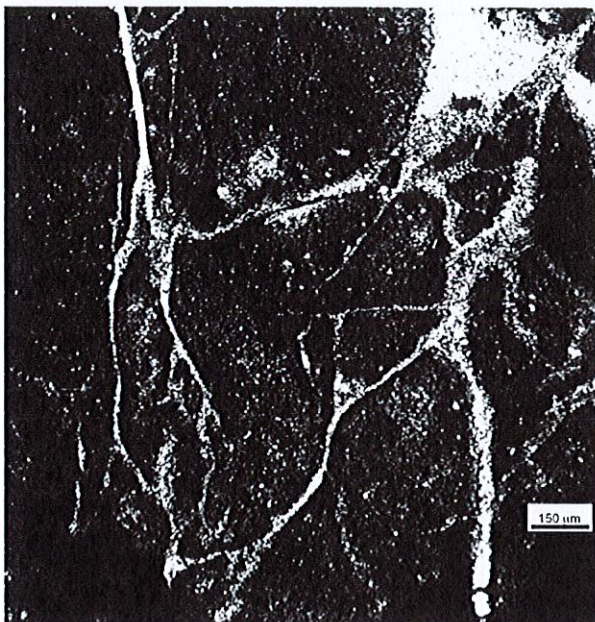


Fig.2 Picture of a thin section prepared for a microprobe analysis showing dark zones of undeformed OPA matrix with dispersed shiny crystals of diffuse calcite. These dark zones are surrounded by veins filled with calcite infillings that can end in calcite concretions such as at the right upper corner of the picture

changes in the deformed structure, or about the geochemical processes that happened in the different microstructures. On the basis of electron microscopic observations, Laurich et al. (2014) discussed the mechanical impact of the progressively increasing deformation in the OPA within and around the fault. Their descriptions focused on thin isolated shear zones and associated slickensides, veins of variable sizes, intensely and densely anastomosed shear zone networks, and independent gouges of various sizes occurring in the faulted sediments. Calcite and celestite infillings of the various microstructures were analyzed, in an initial study, for their major and rare earth elemental contents, and for their Sr isotopic compositions (Clauer et al. 2017a).

The slickensides of the OPA Formation occur in shear zones that are often associated with millimeter-wide veins filled with calcite together, sometimes, with celestite infillings (Fig. 2). These shear zones are internally characterized by a preferential orientation of the clay particles parallel to the shearing, with sizes of only a few tens of nanometers (Laurich et al. 2014, 2018). Local increases of the number of slickensides characterize highly deformed matrices that were called “scaly clays” by Laurich et al. (2017), consisting in fact of numerous anastomosing thin shear zones. The highest strain recorded by the OPA occurs next to the gouges in the Main Fault, where strong foliations wrap clasts of almost intact matrix material. Often optically darker than the undeformed OPA matrix, the gouges could result from

an overall grain-size reduction and a lower content of diffuse calcite than the nearby scaly clays (Laurich 2016; Laurich et al. 2017). This mineralogical change was probably compensated, at least partly, by an illite authigenesis (Clauer et al. 2017b).

The compressive deformation of the Mont Terri anticline began apparently with a 30° dipping ramp that was associated with a small-amplitude fold as the first stage of the fault propagation. The faulting accounts for an approximate 10-m shortening, which corresponds to the present-day geometry of the fault (Nussbaum et al. 2017). As shortening increased along the basal detachment, the Main Fault was passively transported in the hanging wall of the Mont Terri anticline, tilted progressively with a 45° dip toward the SSE. This structural interpretation suggests an early activation of an incipient, internal thrust in the clay-type lithology at the transition between the OPA and Staffelegg stratigraphic units (Fig. 1).

Based on the description of structural features from the Main Fault at the macro- and mesoscales (Nussbaum et al. 2011), the following information is also useful here: the shaly facies consists mainly of dispersed clay minerals (illite, mixed-layered illite–smectite, kaolinite and chlorite), calcite (diffuse or as fossils and micro-veins in the matrix) and quartz (Pearson et al. 2003). The tectonically undeformed fabric is heterogeneous and weakly bedded, with a 15% porosity that increases in the gouges (Nussbaum and Bossart 2008; Houben et al. 2013, 2014). The fracturing network and the strain intensity are heterogeneous within the fault (Nussbaum et al. 2011), comprising zones with thin fault gouges (< 1 cm), C'-type shear bands (*sensu* Passchier 2005), mesoscale and microscale folds, striated fault planes and even undeformed OPA matrix. Estimated from calcite and celestite veins at the Mont Terri (Pearson et al. 2003), the study of the paleo-fluid flux(es) identified advective flows (Nagra 2008). The P–T conditions were found as variable within the fault with a temperature at about 55 °C at the onset of the fault fabric due to an overburden of 1000-m sediments (Mazurek et al. 2006).

More petrographic and geochemical information, mostly about the veins and the calcite dispersed in the OPA matrix, is also available in accessible internal reports (Degueldre et al. 1998; Lancelot, 2001; Pearson et al. 2001, 2003). In addition to diffuse calcite of the OPA matrix, de Haller et al. (2014) analyzed vein wafers (< 1 mm thick) of calcite and celestite with fibrous crack-seal microstructures, the data of which suggest syntectonic precipitations. Those authors interpreted the oxygen and carbon isotopic profiles of the OPA rocks as a result of interactions with ascending fluid flows during the Late-Miocene/Early-Eocene folding. They stated also that the whole OPA acted as a barrier for fluid flows during most of its history except during the considered tectonic–thermal event, but they did not identify what

they consider to be “ascending fluids”, nor how and where these fluids originated, both of these aspects being addressed hereunder.

The sampling and the analytical methods

Most of the fault-zone samples analyzed here belong to cores from BSF-06 and BPS-12 drillings located next to each other, as well as from BIC-A1 drilling (Laurich et al. 2014). The calcite and celestite infillings of the micro-veins were carefully hand separated under a binocular microscope and the pure mineral ships were dissolved straight in dilute acid, while the impure scratched coatings of the slickensides and the gouges were powdered in a mortar and then dissolved in dilute acid. Samples from undeformed OPA matrix and from highly deformed scaly clays were also collected with calcite veins and slickensides, then they were powdered and dissolved in the same type of acid, as well as with diffuse calcite from sediments directly above (samples H2 and SM4 of the Hauptrogenstein and Passwang Formations) and below (samples GWM9 and RM11 of the Staffelegg Formation) the OPA sequence (Table 1). The reason for this varied sampling was assembling a complete set of impacts by tectonic-thermal flowing fluids into microstructural features to be compared to those of the diffusing fluids into the undeformed matrix. In the case of the gouges, the chemical composition of the interactive fluids was expected to be more complex due to a specific pressure-solution impact (Laurich et al. 2014, 2017, 2018). Indeed, fluid–mineral interactions were expected to be different from those in the veins and slickensides, as gouges host also identified authigenic illite and quartz instead of the usual calcite and the more occasional celestite (Clauer et al. 2017b; Laurich et al. 2018).

The cores were collected by air drilling into the floor and the walls of the galleries of the underground laboratory. The resin-stabilized BSF-06 core segment (*cf.* Nussbaum et al. 2006; Fig. 3A) shows anastomosing veins next to the dragged bedding, together with a deformed rock volume parallel to the veins, but without visible bedding (Fig. 3B). Eight micro-vein samples (five calcite and three celestite separates labeled BS10 to BS17; Table 1 and Fig. 3C) were collected and analyzed, as well as the BS1 to BS3 samples of the OPA matrix (Fig. 3B, C). Four BS4 to BS7 matrix samples were collected next to veins to detect and evaluate a potential interaction of the flowing fluids with the host rock along the veins. The BPS-12 core drilled next to the BSF-06 drilling toward the Main Fault contains a 1 cm-thick BP1 gouge collected with two nearby BP2 and BP3 scaly clays taken about 1 and 2 cm away from the gouge sample. Three further BP4, BP7 and BP10 samples of the same gouge were also collected, together with the BP5, BP6, BP8 and BP9 scaly clays next to two of them.

Table 1 Location, description and contents of the major elements and Sr (in µg/g), with the 1/Sr, Ca/Sr and ⁸⁷Sr/⁸⁶Sr ratios of the leached carbonate and sulfate mineral phases from OPA and from sediments around in the Main Fault of the Mont Terri laboratory

| Data of this publication | | | | | | | | | | | | | | | | | | |
|--------------------------|-----------------|------------------------|-----------|-------|-------|------|------|--------|-------|--------|-------|-------|-------|-------|--------------|-------|--|---------------|
| Stratigraphy | Location | Description | Sample ID | Si | Al | Mg | Ca | Fe | Mn | Ti | Na | K | P | Sr | 1/Sr | Ca/Sr | ⁸⁷ Sr/ ⁸⁶ Sr (±2σ × 10 ⁻⁶) | |
| Hauptrogenstein | BDB1 (– 9.7 m) | Matrix | H2-b | 0.001 | 0.001 | 0.08 | 10.2 | 0.01 | 0.002 | – | 0.003 | – | – | 0.009 | 106 | 1083 | 0.707332 (14) | |
| | | Calcite vein | H2-v | 0.01 | 0.008 | 0.02 | 10.8 | 0.10 | 0.005 | – | – | – | – | – | 0.002 | 508 | 5500 | 0.707753 (38) |
| Passwang | BDB1 (– 98.2 m) | Matrix | SM4-b | 0.006 | 0.005 | 0.10 | 9.21 | 0.30 | 0.03 | – | 0.009 | – | 0.009 | 0.01 | 87.0 | 801 | 0.707446 (6) | |
| | | Calcite vein | SM4-v | 0.002 | 0.002 | 0.04 | 7.29 | 0.25 | 0.02 | – | 0.002 | – | 0.001 | 0.01 | 70.6 | 514 | – | |
| Opalinus Clay | BSF-06 | Matrix around vein 5 | BS7 | – | – | – | – | – | – | – | – | – | – | – | – | 31.4 | 0.707596 (5) | |
| | | Calcite of vein 1 | BS10 | – | – | – | – | – | – | – | – | – | – | – | – | – | 0.707763 (8) | |
| | | Celestite of vein 2 | BS12 | – | – | – | – | – | – | – | – | – | – | – | – | – | 0.707767 (5) | |
| | | Celestite of vein 3 | BS14 | – | – | – | – | – | – | – | – | – | – | – | – | – | 0.707768 (9) | |
| | | Calcite of vein 4 | BS15 | – | – | – | – | – | – | – | – | – | – | – | – | – | 0.707798 (8) | |
| | | Calcite of vein 5 | BS16 | – | – | – | – | – | – | – | – | – | – | – | – | – | 0.707605 (6) | |
| | | Celestite of vein 5 | BS17 | – | – | – | – | – | – | – | – | – | – | – | – | – | 0.707605 (14) | |
| Staffelegg | BIC-A1 | Slickenside | BC3 | 0.02 | 0.02 | 0.14 | 8.83 | 0.26 | 0.06 | 0.0004 | 0.11 | 0.04 | 0.004 | 0.11 | 9.30 | 82.1 | 0.707773 (9) | |
| | | duplicate | BC4 | 0.05 | 0.07 | 0.23 | 12.8 | 0.41 | 0.08 | 0.002 | 0.16 | 0.09 | 0.03 | 0.21 | 4.73 | 60.7 | – | |
| | | BC5 | – | – | – | – | – | – | – | – | – | – | – | – | – | – | 0.707728 (6) | |
| | | BC6 | – | – | – | – | – | – | – | – | – | – | – | – | – | – | 0.707746 (8) | |
| | | BC7 | – | – | – | – | – | – | – | – | – | – | – | – | – | – | 0.707747 (5) | |
| | | GWM9-b | 0.04 | 0.04 | 0.32 | 8.48 | 0.17 | 0.03 | – | 0.18 | 0.03 | 0.002 | 0.03 | 0.002 | 0.03 | 35.9 | 304 | 0.707509 (5) |
| | | Matrix | RM11-b | 0.004 | 0.008 | 0.07 | 7.94 | 0.02 | 0.01 | – | 0.08 | 0.008 | 0.006 | 0.07 | 14.5 | 115 | 0.707247 (6) | |
| Opalinus Clay | BSF-06 | Calcite vein | RM11-v | – | 0.001 | 0.06 | 9.81 | 0.03 | 0.02 | – | – | – | – | 0.01 | 131 | 1287 | 0.707697 (4) | |
| | | Undeformed clay matrix | BS1 | 0.03 | 0.02 | 0.24 | 6.90 | 0.25 | 0.03 | 0.001 | 0.20 | 0.07 | 0.01 | 0.03 | 39.8 | 275 | 0.707735 (8) | |
| | | | duplicate | 0.05 | 0.03 | 0.16 | 6.56 | 0.17 | 0.02 | 0.001 | 0.20 | 0.07 | 0.05 | 0.02 | 43.3 | 284 | – | |
| | | | BS2 | 0.04 | 0.04 | 0.28 | 5.75 | 0.18 | 0.03 | 0.001 | 0.34 | 0.11 | 0.03 | 0.04 | 25.3 | 146 | 0.707680 (7) | |
| | | | duplicate | 0.08 | 0.06 | 0.21 | 5.88 | 0.15 | 0.02 | 0.001 | 0.36 | 0.13 | 0.09 | 0.04 | 25.8 | 152 | – | |
| | | | BS3 | 0.03 | 0.02 | 0.12 | 6.57 | 0.18 | 0.02 | 0.001 | 0.14 | 0.05 | 0.03 | 0.02 | 51.5 | 338 | 0.707541 (7) | |
| | | | BS4 | 0.005 | 0.006 | 0.09 | 8.05 | 0.28 | 0.04 | 0.0003 | 0.02 | 0.013 | 0.002 | 0.35 | 2.84 | 22.9 | 0.707768 (4) | |
| | | | BS5 | 0.006 | 0.005 | 0.06 | 5.16 | 0.18 | 0.03 | 0.0002 | 0.02 | 0.009 | 0.001 | 0.10 | 9.79 | 50.5 | 0.707766 (6) | |
| | | | BS6 | 0.02 | 0.01 | 0.08 | 7.10 | 0.22 | 0.03 | 0.0001 | 0.08 | 0.03 | 0.01 | 0.23 | 4.38 | 31.1 | 0.707766 (6) | |
| | | | BS8 | 0.03 | 0.03 | 0.12 | 6.80 | 0.18 | 0.03 | 0.001 | 0.20 | 0.07 | 0.06 | 0.03 | 35.0 | 238 | 0.707686 (7) | |
| | | | BS9 | 0.09 | 0.08 | 0.26 | 6.39 | 0.22 | 0.03 | 0.0002 | 0.64 | 0.20 | 0.16 | 0.04 | 22.5 | 144 | 0.707706 (11) | |
| Calcite of vein 2 | BS11 | – | 0.001 | 0.06 | 7.19 | 0.26 | 0.04 | 0.0003 | 0.003 | 0.001 | 0.001 | 0.94 | 1.07 | 7.66 | 0.707779 (7) | | | |

Table 1 (continued)

| Data of Clauer et al. (2017a) | | | | | | | | | | | | | | | | | |
|-------------------------------|------------------|------------------------------|-----------|-------|-------|------|------|------|------|--------|-------|-------|-------|------|------|-------|---|
| Stratigraphy | Location | Description | Sample ID | Si | Al | Mg | Ca | Fe | Mn | Ti | Na | K | P | Sr | 1/Sr | Ca/Sr | ⁸⁷ Sr/ ⁸⁶ Sr (± 2σ × 10 ⁻⁶) |
| BIC-A1 | | Calcite of vein 3 | BS13 | 0.001 | 0.001 | 0.07 | 9.00 | 0.31 | 0.05 | 0.002 | 0.002 | 0.001 | 0.001 | 0.11 | 9.30 | 83.7 | 0.707767 (3) |
| | | Undeformed clay matrix | BC1 | 0.14 | 0.15 | 0.23 | 6.55 | 0.22 | 0.04 | 0.0007 | 0.36 | 0.27 | 0.03 | 0.03 | 38.7 | 254 | 0.707574 (10) |
| BPS-12 | | Gouge | BP1 | 0.25 | 0.14 | 0.57 | 3.58 | 0.17 | 0.02 | 0.003 | 2.18 | 0.53 | 0.16 | 0.05 | 18.8 | 67.3 | 0.707718 (8) |
| | | | duplicate | 0.25 | 0.12 | 0.55 | 3.29 | 0.16 | 0.02 | 0.003 | 2.15 | 0.51 | 0.14 | 0.05 | 18.8 | 62.0 | - |
| | | | BP4 | 0.87 | 0.43 | 1.57 | 9.77 | 0.56 | 0.05 | 0.01 | 5.23 | 1.00 | - | 0.11 | 9.38 | 91.6 | 0.707735 (17) |
| | | | BP7 | 0.14 | 0.41 | 1.97 | 12.5 | 0.56 | 0.07 | - | 5.46 | 0.69 | 0.09 | 0.04 | 26.9 | 335 | 0.707914 (5) |
| | | | duplicate | 0.08 | 0.06 | 0.19 | 7.95 | 0.28 | 0.05 | 0.001 | 0.39 | 0.13 | 0.09 | 0.03 | 31.6 | 251 | - |
| | | | BP10 | 0.09 | 0.17 | 0.95 | 8.67 | 0.26 | 0.05 | 0.003 | 2.33 | 0.27 | 0.06 | 0.12 | 8.10 | 70.2 | 0.707763 (7) |
| | | | BP5 | 0.06 | 0.05 | 0.14 | 8.61 | 0.28 | 0.06 | 0.001 | 0.20 | 0.04 | 0.012 | 0.02 | 42.9 | 369 | 0.707770 (8) |
| | | | | | | | | | | | | | | | | | |
| | | Sclay clay next to gouge BP4 | BP6 | 0.10 | 0.09 | 0.26 | 10.0 | 0.34 | 0.07 | 0.002 | 0.46 | 0.10 | 0.06 | 0.03 | 30.0 | 300 | 0.707761 (5) |
| | | | BP8 | 0.08 | 0.07 | 0.30 | 8.96 | 0.21 | 0.05 | 0.0008 | 0.55 | 0.08 | - | 0.02 | 55.8 | 500 | 0.707720 (6) |
| | | | | | | | | | | | | | | | | | |
| | BDB1 (- 241.7 m) | Sclay clay next to gouge BP7 | | | | | | | | | | | | | | | |
| | | Slickenside | GW9-s | 0.02 | 0.03 | 0.12 | 7.29 | 0.13 | 0.03 | - | 0.09 | - | - | 0.05 | 22.0 | 160 | 0.707755 (6) |

The table is divided into two parts for the data generated here and for those of Clauer et al. (2017a) publication

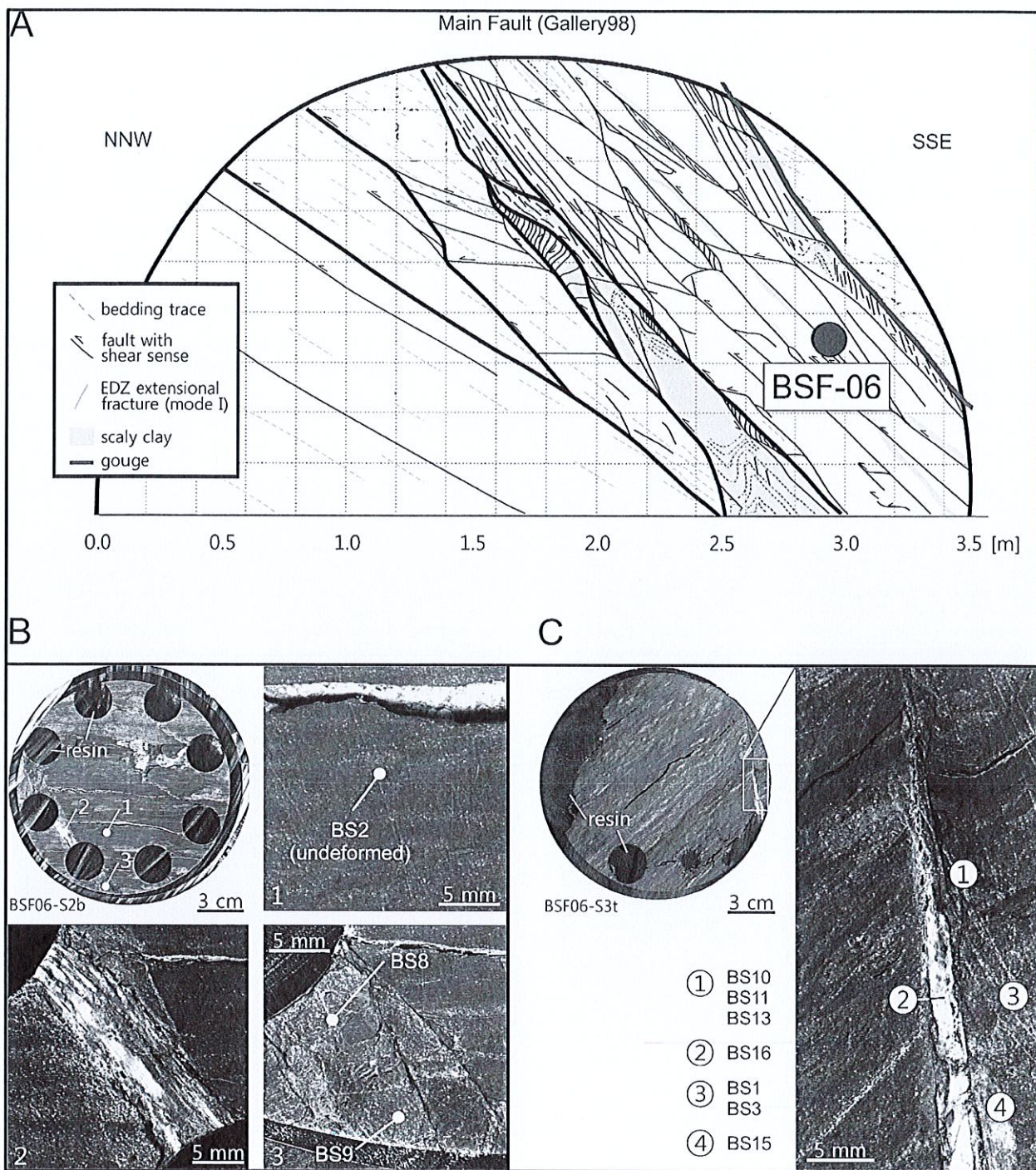


Fig. 3 A Sketch of the outcropping Main Fault in the Gallery 98 of the rock laboratory with the location of the BSF-06 core as a red dot; B, C detailed photographic locations of the calcite and celestite samples from analyzed BSF-06 microstructures

From BIC-A1 core drilled into the floor of the Gallery 08 next to the fault with a vertical orientation to intersect the fault zone below the laboratory, five rock chips BC1 and BC3 to BC7, including an undeformed matrix sample,

were also selected for analysis of the slickenside surfaces of the Staffelegg, Hauptrogenstein and Passwang Formations cut by the drilling underneath the laboratory.

The vein infillings consisted of pristine calcite (CaCO_3) often associated with celestite (SrSO_4). The slickensides occurred as continuous, smooth, non-porous, thin overgrowths covering the host rocks without any detectable porosity even at scanning electron microscope (SEM) resolution. Occasionally, concentrations of sub-euhedral calcite and celestite crystals were observed on the smooth slickenside surfaces with step raisers at the end of linear calcite or celestite occurrences (Fig. 4). Characterized by an XRD lattice spacing of 10 Å, illite was also identified by transmission electron microscopy (TEM) in the gouges (Clauer et al. 2017b; Fig. 5).

The calcite and celestite crystals are known to react very differently to acid leaching: the former is easily dissolved in a weak dilute acid at room temperature, whereas the latter is quite insoluble in most acids, even concentrated. Therefore, a sequential leaching procedure was applied to the hand-picked ships that were hand ground before dissolution for analysis of their elemental and Sr isotopic compositions.

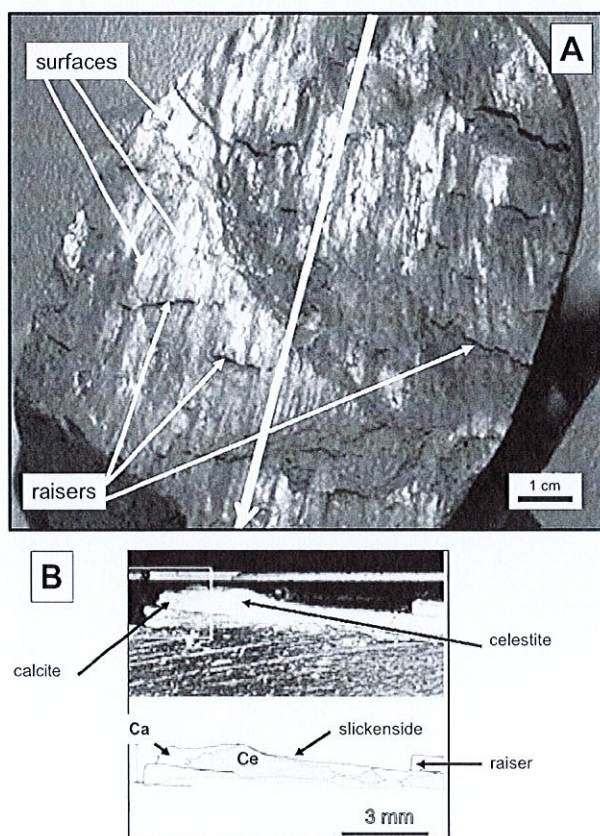


Fig. 4 **A** Photograph of a slickenside surface from a core of drill hole BIC-A1 (modified from Laurich 2016); the plain surfaces and the raisers are indicated by the fine arrows and the bigger white arrow in the center of the oval gives the direction of the water flow; **B** transversal cut of a raiser with the associated celestite and calcite, both sketched below

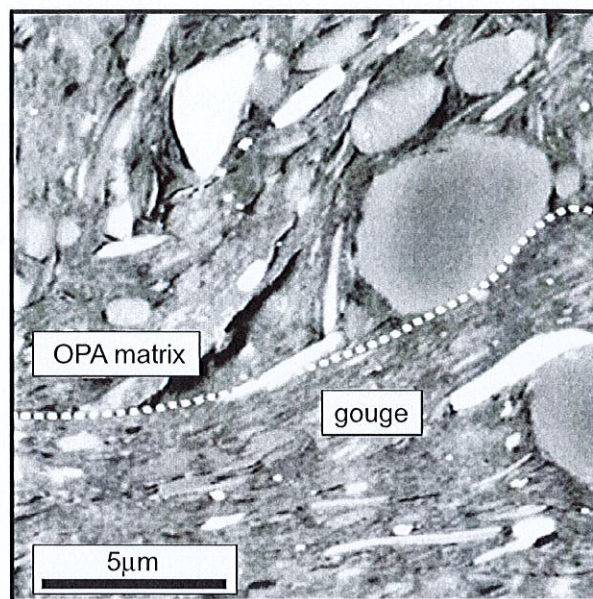


Fig. 5 SEM photograph of the undeformed OPA matrix at the top relative to the immediate gouge: the difference in the grain size is clearly in favor of the matrix (modified from Laurich et al. 2018)

The procedure started with a 10-min, ultrapure 1 N HAc dissolution of the soluble calcite phase, either pure or mixed with celestite. In the case of calcite–celestite mixtures, the remaining celestite fraction was dissolved by a solution consisting of 7 N HNO_3 + 6 N HCl + 12 N HF in a microwave oven (ThermoFisher Thos One) at high temperature and pressure. All obtained solutions were evaporated and dissolved in a few drops of HNO_3 before elemental or Sr isotopic analysis.

The application of the leaching experiments probably needs some quick recalls about their characteristics depending on the types of dissolved minerals. If the samples are vein infillings that consist mostly of calcite, celestite being insensitive to any weak acid leaching, the leachates obtained by an initial weak acid action strictly represent the dissolved calcite, as well as other soluble minerals, together with the adsorbed free elements if any. Salts, but also sulfates and/or sulfides, again if present, may also be dissolved at the same time. Therefore, the contents of elements, such as Na and/or Fe, might be slightly biased by the dissolution of these soluble minerals. In contrast, the $^{87}\text{Sr}/^{86}\text{Sr}$ ratios are not affected by the dissolution of such minerals as they are depleted in Rb and, therefore, did not accumulate radiogenic ^{87}Sr since crystallization.

The Sr purification for the isotope measurements was completed on an Eichrom Sr resin following the procedure described by Pin et al. (2003). After separation, the Sr aliquots were loaded onto a Ta filament and the $^{87}\text{Sr}/^{86}\text{Sr}$ isotopic ratios measured by a solid-source, thermal ionization

mass spectrometer with a multi-collector (Thermo-Finnigan Triton TI). The external reproducibility of the Sr isotopic results was controlled by the repetitive analysis of the NBS-987 standard that had a mean value of 0.710258 ± 0.000002 (2σ) during the time of the study. The contents of Ca and Sr, as well as of Si, Al, Mg, Fe, Mn, Ti, Na, K, P and of the rare-earth elements (REEs) were determined by inductively coupled plasma atomic emission or mass spectrometry (a Jobin Yvon SA JY124 ICP-AES and a Thermo-Electron PQ2 ICP-MS) following the procedure of Samuel et al. (1985). Periodic elemental analyses of the BE-N and GL-O international rock standards set the analytical reproducibility at 3% ($\pm 2\sigma$) for the determinations of the major elements, 5% for those of Sr and 10% for those of the REEs.

Results

The variations of the $^{87}\text{Sr}/^{86}\text{Sr}$ ratios

The diffuse calcite dispersed together with other sulfate and chloride soluble minerals in the undeformed OPA matrix yields $^{87}\text{Sr}/^{86}\text{Sr}$ ratios from 0.70760 to 0.70804 on the basis of the data obtained here and earlier (Clauer et al. 2017a) and of those by de Haller et al. (2014). This scatter is larger than the $^{87}\text{Sr}/^{86}\text{Sr}$ ratios of the diffuse calcite dispersed in the sediments above and below the OPA that scatter from 0.70725 to 0.70751 (Table 1), while those of the calcite and celestite of the micro-veins within the Main Fault range narrower, from 0.70761 to 0.70780. In turn and as an indirect test of the analytical quality when associated next to each other, the calcite and celestite ships extracted from the same veins (in the case of the BSF-06 core) yield systematically identical $^{87}\text{Sr}/^{86}\text{Sr}$ ratios within analytical uncertainty. The

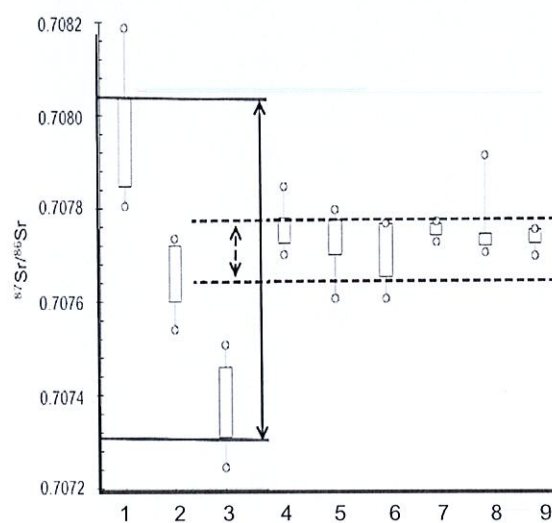
$^{87}\text{Sr}/^{86}\text{Sr}$ ratios of the nearby slickenside extracts are in the same range, from 0.70773 to 0.70777, as are those of most leachates from gouges with values from 0.70772 to 0.70776 (Fig. 6). In fact, only the result of the leachate from BP7 gouge is analytically off this range with the highest $^{87}\text{Sr}/^{86}\text{Sr}$ ratio of the gouge leachates at 0.70791. The $^{87}\text{Sr}/^{86}\text{Sr}$ ratios of the calcite crystals from slickenside surfaces are also very homogeneous, whereas the calcite dispersed in the matrix that embed the veins yields $^{87}\text{Sr}/^{86}\text{Sr}$ ratios that are slightly more radiogenic than those of the dispersed calcite from the plain OPA matrix. The scaly clays yield $^{87}\text{Sr}/^{86}\text{Sr}$ ratios in the range of the diffuse calcite of the matrix, but this more restricted data scatter clearly depends on the respective amounts of the undeformed and deformed material mixture of each analyzed scaly clay sample and, therefore, most probably on how the samples were collected. The $^{87}\text{Sr}/^{86}\text{Sr}$ ratios of the calcite dispersed in the sediments from above and below the OPA are also outside the range of the values from diffuse calcite of the OPA matrix, whereas those of the calcite from veins of the framing formations are within the range of the calcite vein infillings of the OPA within the Main Fault.

Combined with de Haller et al.'s (2014) Sr isotopic data of calcite leached from undeformed OPA matrix and from veins of the Main Fault, the $^{87}\text{Sr}/^{86}\text{Sr}$ ratios obtained here on vein and slickenside infillings, in and close to the fault, range very narrowly between 0.70768 and 0.70778, with a very few values either below or above the box-plotted data (Fig. 6).

The contents of the major elements

The concentrations of most major elements from calcite dispersed in the undeformed OPA matrix and in the intensely

Fig. 6 Box plots of the $^{87}\text{Sr}/^{86}\text{Sr}$ ratios from the diffuse and microstructural calcite and celestite infillings of the OPA and the surrounding sediments (from 3 to 8) with the data of de Haller et al. (2014) (for 1 and 2) and of Clauer et al. (2017a); The central rectangle of the box plots represents 75% of the analyses with a transversal bar for the average of these data, the highest and lowest values being outlined by circles above and below the box. The double dashed line frames the $^{87}\text{Sr}/^{86}\text{Sr}$ ratio of most microstructures



- 1: dispersed calcite from undeformed OPA (A)
- 2: dispersed calcite from undeformed OPA (B)
- 3: diffuse calcite from surrounding sediments (B)
- 4: calcite of veins in OPA (A)
- 5: calcite of veins in OPA (B)
- 6: celestite of veins in OPA (B)
- 7: slickensides in OPA (B)
- 8: gouges in OPA (B)
- 9: veins in surrounding sediments (B)

deformed scaly clays, together with the calcite infillings of the slickensides, veins and gouges yield significant variations (Table 1). Some Ca data show widely varying contents from 3.3 to 12.8 mg/g and, among the other elements, Si exhibits also large variations from about 0.001 to 0.14 mg/g in the leachates of the OPA matrix and of the micro-tectonic features, whereas its contents are significantly higher, from 0.09 to 0.87 mg/g, in the gouges where quartz authigenesis was observed. The K contents are also widely scattered from very low 0.001–0.03 mg/g levels in the calcite of the veins and of the OPA matrix around the veins, to 0.20 mg/g in the leachates of the rock matrix, the scaly clays and the slickensides, even reaching 1.0 mg/g in those of the gouges where illite authigenesis was detected. The same trends were observed for Na and Mg with, again, significantly higher contents in the gouge leachates.

The Ca/Sr ratio of the calcite dispersed in the undeformed OPA matrix ranges from 146 to 338, whereas that of the calcite infillings of the veins and of the OPA matrix wrapping the veins is significantly lower from 7.7 to 84 due to higher Sr contents. The leached OPA matrix sampled away from microstructures and from the scaly clays yields significantly higher Ca/Sr ratios (> 100) than the calcite of the microstructures and of the OPA matrix closely around the veins. That of the gouges ranges from 62 to 92, except for sample BP7 which Ca/Sr ratio is far higher at 335.

The contents and distribution of the REEs

The distribution patterns of the REEs from local microstructural infillings have already been published, but not the corresponding numerical data (Table 2). The calcite infillings of the veins yield the lowest total REE contents from 1.0 to 1.3 mg/g, whereas those of the calcite dispersed in the undeformed OPA matrix range from 3.2 to 5.3 $\mu\text{g/g}$, together with the 1.1 to 2.7 $\mu\text{g/g}$ of those from the matrix closely around the veins. The wide ranges, from 1.3 to 5.8 mg/g, of the REEs contents leached off the gouges confirm a more complex evolution than for the other microstructures. In turn, the calcite infillings of the veins are depleted in REEs relative to the dispersed calcite of the undeformed matrix, whereas the other micro-features contain infillings slightly enriched in REEs.

Among the specific characteristics of the REEs, it is probably appropriate to recall briefly that they are lithophile, electropositive, mostly trivalent and refractory, which means that they are not preferentially concentrated by any type of fluid, but rather stay in mineral structures or are adsorbed at their surface. Their application in geochemistry is based on their changing ionic radius, as well as on the capacities of two of these elements to modify their redox state: cerium as Ce^{3+} and Ce^{4+} , and europium as Eu^{2+} and Eu^{3+} . Also, REE patterns characterizing sedimentary materials are often very

uniform as they are representative of the upper continental crust (e.g., Taylor and McLennan 1985), which is easily identified by a negative Ce anomaly due to varied oxidation–reduction conditions and a more or less positive Eu anomaly that is often related to some partitioning of progressively altered detrital plagioclases. In this context, seawater is generally characterized by a marked Ce depletion due to an oxidation into Ce^{IV} and its separation from other REE by preferential uptake onto Mn^{IV} oxide.

The changes in the REEs of geological materials are often visualized by the comparison of their respective contents with those of a standard/reference rock (e.g., Piper and Bau, 2013). In an earlier study (Clauer et al. 2017a), the REE distribution patterns from infillings of the various microstructures were compared to those of the dispersed calcite from undeformed OPA matrix to visualize the differences among these materials. For younger sedimentary materials, they are generally compared to either those of the North American Shale Composite (NASC; Gromet et al. 1984) or to those of the post-Archaean Australian Shales (PAAS; Taylor and McLennan 1985). Compared here to the PAAS reference, the patterns of the undeformed OPA leachates in and around the fault are quite similar and regular in their shape with an increasing trend from La to Eu and a regular decreasing trend until Lu (Fig. 7A). Only the Gd content of the duplicate analysis of the matrix BS1 is clearly too low, suggesting an analytical problem. The next diagram outlines the patterns of the gouges that are similar to those of the undeformed matrix (Fig. 7B) with an increasing trend from La to Eu as the most concentrated and a linear decreasing trend from Eu until Lu. In detail, the Eu ratio monitors the shape of the distribution, as some of the leachates yield only a limited increase.

As a preliminary wrap-up, it can be stated that the patterns of the gouges mimic quite well those of the undeformed OPA, which suggests that the majority of the constitutive soluble minerals of the gouges provide a similar pattern than that of the initial OPA matrix with, however, a slightly enlarged summit of the pattern on both sides of Eu. The patterns of the scaly clays relative, again, to the PAAS distribution, are quite similar to those of the undeformed OPA matrix with an identical enlargement of the summit when the total REE contents decrease (Fig. 7C). The patterns of the two leached slickenside surfaces provide again similar patterns with an increase from La to Eu and a regular decrease from Eu to Lu (Fig. 7D). The positive anomaly of Eu is again variable and suggests, as for the gouges, that the leachates consist mostly of a distribution identical to those of the initial OPA. In contrast, the patterns of the calcite from the veins are clearly different with no Eu anomaly, but instead a straight linear increase from La to Er and a linear decrease beyond (Fig. 7D). As expected, this different pattern confirms that the infillings of the veins are of a different

Table 2 REE contents (in µg/g) of the studied carbonate and sulfate infillings extracted from OPA and associated sediments in the Main Fault of the Mont Terri laboratory

| Data of this publication | | | | | | | | | | | | | | | | | | | | |
|--------------------------|------------------|-------------------------------|-----------------|--------------|------------|------|------|-----|-----|-----|-----|-----|----|-----|----|----|------|-----------|----|-----------|
| Stratigraphy | Location | Description | Sample IDs | La | Ce | Pr | Nd | Sm | Eu | Gd | Tb | Dy | Ho | Er | Tm | Yb | Lu | Total REE | | |
| Opalinus Clay | BSF-06 | Undeformed clay matrix | BS1 | 477 | 1334 | 159 | 683 | 13 | 32 | 134 | 19 | 106 | 19 | 51 | 6 | 38 | 5 | 3203 | | |
| | | | Duplicate | 555 | 2114 | 234 | 1081 | 235 | 54 | 214 | 30 | 154 | 26 | 69 | 8 | 46 | 6 | 4827 | | |
| | | | BS2 | 436 | 1487 | 202 | 925 | 199 | 48 | 194 | 27 | 143 | 25 | 64 | 7 | 43 | 6 | 3804 | | |
| | | | Duplicate | 459 | 2167 | 267 | 1314 | 305 | 71 | 275 | 38 | 188 | 31 | 78 | 8 | 49 | 7 | 5256 | | |
| | | BS3 | 538 | 1729 | 191 | 838 | 171 | 39 | 169 | 23 | 119 | 21 | 58 | 7 | 42 | 6 | 3952 | | | |
| | | BS4 | 206 | 672 | 84 | 346 | 63 | 18 | 73 | 13 | 82 | 17 | 50 | 6 | 38 | 5 | 1674 | | | |
| | | BS5 | 142 | 441 | 50 | 233 | 42 | 12 | 49 | 8 | 51 | 11 | 31 | 4 | 23 | 3 | 1099 | | | |
| | | BS6 | 306 | 1170 | 136 | 585 | 114 | 31 | 124 | 19 | 112 | 22 | 65 | 8 | 46 | 7 | 2744 | | | |
| | | BS8 | 493 | 2156 | 251 | 1177 | 256 | 60 | 232 | 33 | 174 | 30 | 79 | 9 | 54 | 7 | 5012 | | | |
| | | BS9 | 431 | 2348 | 300 | 153 | 367 | 86 | 320 | 44 | 216 | 35 | 87 | 9 | 52 | 7 | 5833 | | | |
| | | BP1 | 89 | 460 | 77 | 424 | 123 | 26 | 96 | 12 | 52 | 8 | 19 | 2 | 11 | 1 | 1401 | | | |
| | | Duplicate | 83 | 420 | 71 | 390 | 112 | 24 | 86 | 11 | 47 | 7 | 17 | 2 | 10 | 1 | 1280 | | | |
| | | BP4 | 223 | 1063 | 170 | 920 | 253 | 53 | 217 | 23 | 113 | 17 | 37 | 3 | 23 | 3 | 3120 | | | |
| Staffellegg | BDB1 (– 241.7 m) | Slickenside | BP7 | 394 | 1989 | 317 | 1700 | 463 | 100 | 386 | 46 | 211 | 31 | 71 | 9 | 43 | 6 | 5766 | | |
| | | | BP10 | 329 | 1500 | 219 | 1099 | 279 | 60 | 239 | 28 | 138 | 21 | 51 | 6 | 32 | 5 | 4005 | | |
| | | | BP5 | 500 | 1702 | 195 | 862 | 184 | 41 | 173 | 22 | 121 | 21 | 55 | 7 | 42 | 5 | 3930 | | |
| | | | BP6 | 567 | 2088 | 260 | 1183 | 266 | 59 | 241 | 30 | 161 | 27 | 70 | 8 | 51 | 7 | 5018 | | |
| | | BP8 | 488 | 1773 | 208 | 916 | 203 | 45 | 185 | 24 | 130 | 22 | 58 | 7 | 47 | 6 | 4110 | | | |
| | | GW9M9-s | 246 | 564 | 75 | 307 | 58 | 14 | 61 | 9 | 62 | 13 | 38 | 5 | 33 | 5 | 1489 | | | |
| | | Data of Clauer et al. (2017a) | | | | | | | | | | | | | | | | | | |
| | | Stratigraphy | Location | Description | Sample IDs | La | Ce | Pr | Nd | Sm | Eu | Gd | Tb | Dy | Ho | Er | Tm | Yb | Lu | Total REE |
| | | Hauptrogenstein | BDB1 (– 9.7 m) | Matrix | H2-b | 261 | 318 | 49 | 209 | 42 | 10 | 48 | 6 | 39 | 8 | 23 | 3 | 17 | 2 | 1037 |
| | | | | | H2-v | 185 | 217 | 31 | 134 | 25 | 6 | 33 | 5 | 31 | 7 | 21 | 2 | 16 | 2 | 717 |
| | | | | Calcite vein | SM4-b | 100 | 226 | 24 | 88 | 15 | 4 | 16 | 2 | 15 | 3 | 10 | 2 | 11 | 2 | 516 |
| | | | | | SM4-v | 136 | 295 | 3 | 120 | 20 | 5 | 19 | 3 | 18 | 4 | 12 | 2 | 13 | 2 | 681 |
| | | Passwang | BDB1 (– 98.2 m) | Matrix | BS11 | 125 | 383 | 50 | 212 | 40 | 13 | 55 | 10 | 66 | 15 | 43 | 5 | 29 | 4 | 1049 |
| BS13 | 161 | | | | 475 | 61 | 258 | 48 | 15 | 67 | 12 | 80 | 18 | 52 | 6 | 35 | 5 | 1293 | | |
| Calcite vein | BC3 | | | 412 | 1452 | 183 | 794 | 156 | 38 | 153 | 24 | 138 | 26 | 69 | 9 | 51 | 7 | 3511 | | |
| | Duplicate | | | 664 | 2492 | 329 | 1459 | 312 | 73 | 286 | 42 | 236 | 42 | 112 | 13 | 81 | 11 | 6153 | | |
| Opalinus Clay | BSF06 | Calcite of vein 2 | GW9M9-b | 329 | 734 | 100 | 432 | 89 | 20 | 89 | 12 | 71 | 13 | 38 | 5 | 32 | 4 | 1970 | | |
| | | | RM11-b | 412 | 375 | 47 | 213 | 45 | 11 | 51 | 7 | 41 | 8 | 22 | 3 | 20 | 3 | 987 | | |
| | | Calcite of vein 3 | RM11-v | 24 | 44 | 5 | 23 | 4 | 1 | 7 | 1 | 6 | 1 | 4 | 1 | 3 | 1 | 125 | | |
| | | | | | | | | | | | | | | | | | | | | |
| Staffellegg | BDB1 (– 241.7 m) | Matrix | | | | | | | | | | | | | | | | | | |
| | | | | | | | | | | | | | | | | | | | | |
| | | Calcite vein | | | | | | | | | | | | | | | | | | |
| | | | | | | | | | | | | | | | | | | | | |

Again, the table is divided into two parts for the data generated here and for those released by Clauer et al. (2017a)

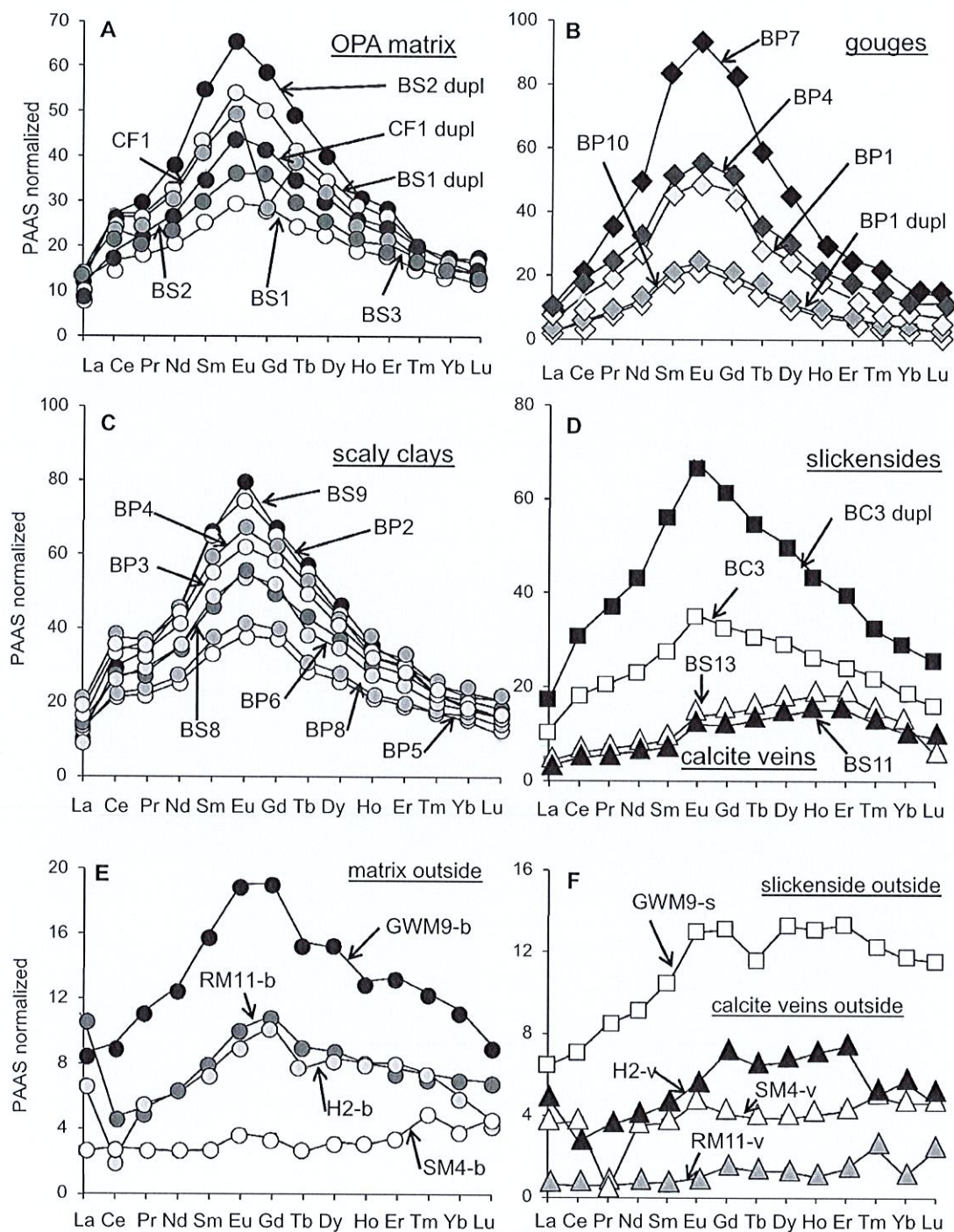


Fig.7 REES distribution patterns relative to the PAAS reference for: **A** the analyzed OPA matrix leachates; **B** the analyzed gouge leachates; **C** the analyzed scaly clays; **D** two slickensides and two calcite

of vein infillings; **E** four matrix leachates outside the OPA; and **F** one slickenside and three calcite veins outside the OPA

origin than the REEs of the surrounding host rocks. Also to be noticed is the fact that the REE contents of the vein infillings are significantly lower than those of the host rocks, which explains, at least partly, that an addition of external

fluids is not easily distinguishable from whole contents of the leachable minerals from OPA matrix.

The REE distribution patterns of the calcite from undeformed matrix of the nearby rock formations, still relative

to the PAAS reference, are expectedly more dispersed than those of the OPA matrix as the origin of the components is not necessarily identical (Fig. 7E). Some of their patterns are either flat or of low ratios, or they increase slightly on the side of the light REEs and slightly decrease on that of the heavy REEs. The few micro-features from outside the OPA give flat patterns for the calcite veins with low contents as those from inside the OPA (Fig. 7E), confirming in turn no chemical relation with the host rocks. The slickenside surfaces contained REEs with increasing light REE trends and irregular trends toward the heavy REEs beyond Eu.

Discussion

The elemental and Sr isotopic identities or differences of the infillings from micro-tectonic features relative to the dispersed calcite from undeformed OPA host sequence and from that of the nearby undeformed sediments in, around and outside the fault system are essential to validate the origin of the interactive fluids and their interactions with the minerals. For instance, the Si, Al, K, Na and Mg contents of the leachates suggest, together with the Ca/Sr ratios, variable elemental compositions for the dispersed calcite of the undeformed OPA matrix relative to that of the microstructures (Table 1). As already stated, some of the differences could be due to the dissolution of other soluble minerals, as is the case in the gouges where the XRD and EDX data indicate that they contain less calcite than the other microstructures, replaced by other newly crystallized minerals (Laurich et al. 2014; Orellana et al. 2017). The chemical compositions of the dissolved minerals suggest also that the interacting fluids in the gouges were different from those of the veins, even if the Ca/Sr ratios of the gouge leachates remain within the values of those from infillings of the other microstructures. While the Ca/Sr ratio is clearly high for the undeformed OPA matrix and for the scaly clays close or not to the gouges (Fig. 6) that of the calcite from other microstructures is clearly lower. As all microstructures are characterized by calcite infillings basically enriched in Ca, any low Ca/Sr ratio has then to be due to abnormal high Sr contents. The low Ca/Sr ratios of the gouge leachates suggest then that they could have been modified by addition of external fluids favoring the crystallization of Sr-rich minerals that grew also in these gouges during the faulting event.

The leachates of the gouges also yield Si/Al ratios different from those of the other microstructures. While the data points of the Si/Al ratio from vein and slickenside infillings plot along a straight line with an origin at the intersection of the coordinates, the data points of the leached gouges plot clearly off this line, right in the field of the theoretical illite Si/Al ratio (Fig. 8A), which confirms the expected illite authigenesis in the gouges, as reported in studies of larger

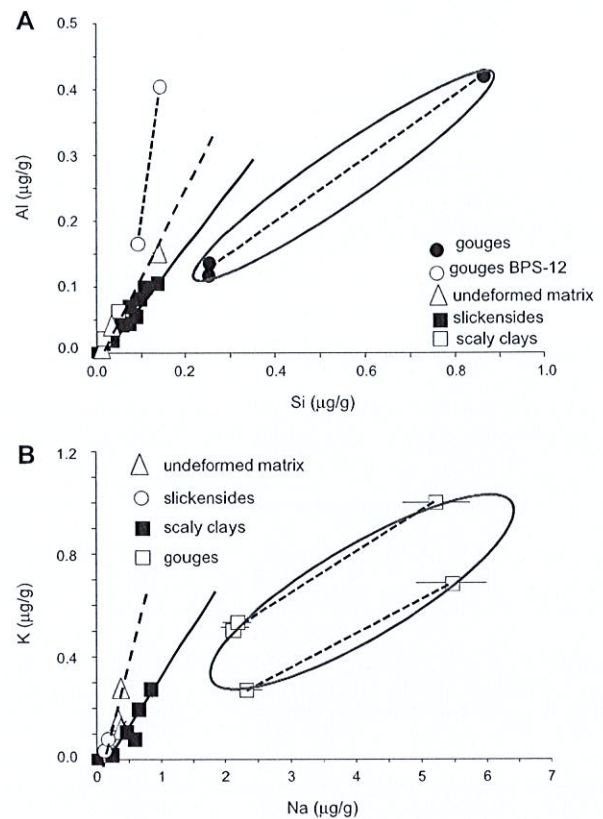


Fig. 8 A The correlated contents of the leached Si and Al from microstructures, from bulk OPA matrix and from sediments above and below (modified from Clauer et al., 2017a). The gouge samples are circled in red; B the correlated contents of the leached K and Na from microstructures, from bulk OPA and sediments above and below. The Na and K contents of the gouge samples are also circled in red

gouges (e.g., Rieder et al. 1998; Vrolijk and Van der Pluijm 1999; Sasseville et al. 2008). The two additional Si/Al data points of the gouge leachates located above the line of the Si/Al ratios for the other microstructures suggest a Si deficit in the leachate that removed these data points from theoretical Si/Al ratio of illite. This result raises another interesting aspect for the gouge volumes: illite authigenesis seems not to occur randomly in all gouges, but rather only at specific conditions that remain to be identified.

The relation between K and Na raises also some concerns, for instance about the correlative ratios of all microstructural infillings having their data points on a straight line with an origin at the intersection of the two coordinates (Fig. 8B). This distribution confirms either an interaction with a different type of fluid(s) in the gouges, or a different interaction of the same fluid(s) with different minerals. The data points of the gouge leachates below the correlation line of the Na and K contents from other microstructures suggest high Na and K contents. As just discussed, the highly soluble K contents

suggest favorable conditions for an illitization, while those of Na most probably result from dissolution of salt crystals that seem to have crystallized in the gouges and/or closely in their wall materials.

The identical $^{87}\text{Sr}/^{86}\text{Sr}$ ratios of the calcite and celestite infillings from the veins confirm that they crystallized from fluids with identical Sr isotopic signatures, but with variable bi-carbonated and sulfated contents, therefore most probably not simultaneously. The undeformed OPA within the Main Fault contains leachable $^{87}\text{Sr}/^{86}\text{Sr}$ ratios that are close to those of the microstructures, suggesting in turn that the undeformed matrix in the fault was also “contaminated” by flowing fluids that leaked into the adjacent host matrix around the veins and the slickensides. Essentially, the process is not a diffusion of local pore waters from undeformed matrix into the microstructures, but a transfer the other way around, e.g. a leak from veins into the undeformed host matrix. Conversely, the $^{87}\text{Sr}/^{86}\text{Sr}$ ratios of the diffuse calcite from undeformed matrix outside the Main Fault are more widely spread (Fig. 6), which calls for two comments: (1) the $^{87}\text{Sr}/^{86}\text{Sr}$ ratios of the dispersed calcite from OPA matrix sampled within the volume of the Main Fault are closer to those of the microstructural infillings than to those of the same matrix outside the fault, and (2) the vein infillings from outside the Main Fault contain Sr with $^{87}\text{Sr}/^{86}\text{Sr}$ ratios that are within the dispersion range of those of the microstructural infillings in the fault and those of most gouge leachates. Similarly, the $^{87}\text{Sr}/^{86}\text{Sr}$ ratios of the calcite from tectonic microstructures of the surrounding sediments are within the range of the $^{87}\text{Sr}/^{86}\text{Sr}$ ratios of the veins, the slickensides and the highly deformed scaly clays, which confirms that the same flowing fluids migrated also along these features (Fig. 6).

The fact that the infillings of all veins and slickensides yield analytically identical $^{87}\text{Sr}/^{86}\text{Sr}$ ratios indicates that the flowing fluids carried Sr with an isotopic signature of a probable unique origin with no detectable addition. Clearly, none of the Sr supplied to the microstructural infillings of the fault system originated in, or interacted extensively with the matrix of the shaly OPA, and/or with the matrix of the surrounding sediments. Distinction between flowing fluids in the microstructures and local diffusion of pore waters in the OPA matrix is also visible in the REE distribution patterns relative to those of the PAAS or the OPA matrix (Clauer et al. 2017a). The difference holds also for the microstructures of the sediments surrounding the OPA, the calcite of which displaying a slightly continuously increasing trend, as well as for the gouge leachates with a positive Sm anomaly relative to the undeformed OPA matrix (Clauer et al. 2017a) that suggests an organic supply (e.g., Piper and Bau 2013). As no positive Sm anomaly has been detected

in any infilling from the other tectonic microstructures relative to the OPA matrix or the PAAS, this REE was necessarily supplied from outside the gouges and probably not from widely around as REEs generally avoid the fluids. This supply may then result from specific location of the gouges at the fault surface where the fluid activity was probably the strongest with, consequently, a larger supply of external elements and more extensive mineralogical changes in this fault sole volume. Interestingly, the Sm anomaly indicative of an organic supply relative to the leachates of the OPA matrix correlates positively with higher P contents in the gouges, which confirms an organic supply. The patterns of the scaly clays are very similar to those of the OPA matrix and to those of the gouges relative to the OPA matrix, when compared to the PAAS reference. The shape of the patterns may, then, depend on the location of the samples relative to the fault plane, and on their constitutive volumes of undeformed and highly deformed materials.

The geochemical contribution to the structural interpretation

Calcite of the undeformed OPA and the surrounding sediments yields $^{87}\text{Sr}/^{86}\text{Sr}$ ratios ranging quite widely from 0.70754 to 0.70774 and from 0.70725 to 0.70751, respectively. By contrast, the $^{87}\text{Sr}/^{86}\text{Sr}$ ratio of the varied microtectonic infillings from different host rocks range narrowly at 0.70774 (± 0.00001). If the $^{87}\text{Sr}/^{86}\text{Sr}$ ratios of the calcite (and celestite) from vein and slickenside infillings trace one single fluid from which they precipitated, the calcite from plain matrices resulted necessarily from diffusing fluids involved in local and probably independent diagenetic interactions and away from the faulting system. In the $^{87}\text{Sr}/^{86}\text{Sr}$ diagram summarizing all measured $^{87}\text{Sr}/^{86}\text{Sr}$ ratios from different collected samples (Fig. 6), most data points of calcite (and celestite) from veins, slickensides and gouges plot above the values of the leachates from nearby and surrounding OPA undeformed matrix associated sediments. Part of the Sr from constituting minerals of the gouges could have originated from variously altered detrital minerals that were somehow grinded by sliding along the fault surface and subjected to a related temperature increase, which confirms in turn that the gouges represent a different “piece” of the local and regional path-flow system with a different function than the veins and the slickensides and more changes in the final mineral composition.

In the calcite and celestite infillings of the veins and the slickensides

Fibrous and laminated features suggest a synkinematic precipitation of calcite and celestite in the veins probably due

to crack-seal processes during shearing (Koehn and Passchier 2000). However, because of the specific crystallization conditions of each, these two minerals had to precipitate successively during the same event, supported by the fact that celestite crystallization needs a higher pressure and salinity (Rimstidt 1997). This delay is most probably due to a changing fluid chemistry, since its precipitation needs also a lower ambient temperature. Therefore, in contrast to de Haller et al. (2014) who suggested that celestite precipitated by interaction of externally sourced Sr from sulfate-rich clay minerals, its precipitation resulted here more probably from a combined alteration of pyrite and calcite, both being also visible in the gouges (Clauer et al. 2017a).

In sum, most microstructural features within and around the fault extension contain infillings that yield identical Sr isotopic signatures. This identity calls for a large initial volume of fluids that flew throughout these microstructures and those of the surrounding sediments during the earlier tectonic event, while the fluids associated with the event studied here reused the initial drains and slickensides, picking up the Sr isotopic of the initial infillings by discretely dissolving some (Nussbaum et al. 2017). Although the $^{87}\text{Sr}/^{86}\text{Sr}$ ratios of calcite (and celestite) of most veins and slickensides are identical, this is not the case for their elemental compositions. The same $^{87}\text{Sr}/^{86}\text{Sr}$ ratio of the infillings, together with the expectedly important involved volume of the flowing fluids, suggests that: (1) these initial fluids originated in a large pool because of the important volume of deposited infillings, and were probably of a marine origin because of the uniform $^{87}\text{Sr}/^{86}\text{Sr}$ ratio, and (2) based on the intrinsic value of the Sr isotopic signature, they originated mainly during the first deformation episode in the Rhine Graben. Apparently, the flowing fluids of the late event reacted extensively with minerals that were lacking radiogenic ^{87}Sr , as their Sr isotopic composition remained homogeneous in the infillings of all veins and slickensides during an extremely long period of millions of years between the two tectonic–thermal events. On the other hand, the noticeably varied chemical composition of these infillings tells that they had varied interactions along their migration path in the micro-drains, especially with sensitive minerals depleted in Rb and, therefore, in radiogenic ^{87}Sr . Minerals such as carbonates, sulfates and salts were then part of the infilling minerals of the microstructures generated during the initial tectonic–thermal event.

In the leached scaly clays and the OPA matrix around the veins

The OPA matrix closely around the microstructural veins yields $^{87}\text{Sr}/^{86}\text{Sr}$ ratios that range between the values of the calcite from undeformed OPA and those of the calcite infillings from veins and slickensides. The values of the Ca/Sr

ratios were also found in-between those of the undeformed matrix and the micro-features. A mixing of two Sr supplies, one from flowing fluids that precipitated calcite in the microstructures, the other from surrounding undeformed matrix with a more scattered Sr isotopic signature, can no longer be denied (Fig. 6). Clauer et al. (1989) analyzed the $^{87}\text{Sr}/^{86}\text{Sr}$ ratio of a calcite vein intruding a carbonate host rock and found evidences for interactions of both the vein fluids and host-rock minerals right next to the vein. The REE patterns of the “contaminated” matrix that wraps the veins confirm a partial chemical intrusion of flowing fluids from veins into the matrix (Clauer et al. 2017a). This result confirms clearly that no detectable pore fluids from the OPA matrix contributed to the flowing fluids, but that the diffusion process was locally the reverse.

The highly deformed OPA scaly clays contain many veins and slickensides that occur closely next to each other. Since they consist visually of undeformed matrix flakes that are less than 300 μm thick and are bound by thin shear zones in the faulted matrix (Laurich et al. 2014), they seem to result tectonically from shear bands changing progressively into meso- and micro-folds (Nussbaum et al. 2011). Their local alteration by incoming fluid flows is confirmed by the $^{87}\text{Sr}/^{86}\text{Sr}$ ratios of the leachates that are often similar to those of either the vein infillings, or the dispersed calcite from matrix closely enveloping the veins. The REE patterns of the leached scaly clays support this discrepancy, as they are mostly similar to those of the leached OPA matrix, while some are similar to the vein calcite. In fact, a link with the tectonically deformed matrix was not really expected as the patterns suggest that despite a visible deformation, the geochemical identity of the scaly clays remains close to that of the leached undeformed matrix, the impact appearing more physical than chemical. On the other hand, Arch et al. (1988) demonstrated that high water contents lead to an increased complexity in shear zones, in which clays benefit from the impact of the flowing fluids, rather than from local pore fluids. In fact, it still looks like the data depend on how sampling was completed with more or less undeformed or deformed collected material.

In the gouges

As already stated, frictional sliding and associated abrasion are common mechanisms affecting gouges, the constituting minerals being often of smaller size than those of the nearby matrix due to this combined physical aspect (Fig. 5). In fact, grinding combines cataclasis with dissolution/precipitation reactions probably driven mostly by pressure solution. Such processes induce also recrystallization of kinked and folded detrital clay particles (Urai et al. 1980), which suggests a combination of external flowing fluids with those released by the local pressure-solution mechanisms that favors illite

authigenesis, for instance, as already described in larger gouges (e.g., Vrolijk and van der Pluijm 1999; Sasseville et al. 2008). Triggered by these chemical aspects, mineralogical changes such as increasing contents of clay and quartz replace the leached calcite in the Main Fault (Laurich et al. 2014; Clauer et al. 2017b; Orellana et al. 2017). In fact, it looks like mineral grinding in the gouge volumes of the fault sole induces here a pressure-solution process with specific mineralogical changes, such as precipitation of illite, salt, gypsum and celestite, however, not in all gouges considering the Si/Al ratio (Clauer et al. 2017b). Clearly, such changes did also not occur in “closed” gouge volumes, as an external supply is needed to explain the abnormally high Sm contents of organic origin. Such organic Sm may have originated in the Rietheim Member of the Staffelegg Formation, which is part of the sliding fault sole (Nussbaum et al. 2017), as it is regionally described as a bituminous schist consisting of shales that host and could have, therefore, released organic- and P-rich fluids into the friction zone during the motion of the fault.

In summary, various geochemical interactions occurred in the gouges. From a geochemical point of view, the resulting leachates yield $^{87}\text{Sr}/^{86}\text{Sr}$ and Ca/Sr ratios that suggest interactions with fluids different from those of the veins and the slickensides. Therefore, they hosted mineral alterations (e.g., dissolutions and neoformations) that did not occur in the other micro-features or in the undeformed matrix around. The varied mineral authigeneses suggest that the residence time of the flowing fluids was also longer in the gouges than in the veins or the slickensides, while their specific location in the fault probably enhanced mineral-fluid interactions aided by pressure-solution processes. For instance, the high Si, Al, K and Na contents of the gouge leachates resulted from natural alteration of original constitutive minerals induced by cataclasis and enriched by organics from outside. Also of importance, salts such as NaCl observed by SEM in the gouges were not detected in the other microstructures, while these increased Na contents in the gouge leachates are not contradicting unchanged $^{87}\text{Sr}/^{86}\text{Sr}$ ratios since salts are not specifically enriched in radiogenic ^{87}Sr over time.

Detailed observations combined with supportive analytical data show that the gouges consist of clasts from OPA matrix mixed with highly altered materials split by tiny shear zones such as in the scaly clays (Laurich 2016). A reasonable postulate is then that changing $^{87}\text{Sr}/^{86}\text{Sr}$ ratios and elemental signatures of gouge leachates resulted from variably lasting interactions relative to limited interactions in the veins and slickensides. In the latter, the continuous fluid flow could not interact beyond a discrete dissolution of the already existing infillings. In summary, the elemental compositions of the soluble phases from gouges did not result only from leaching by flowing fluids, such as in the veins and slickensides, but from longer lasting interactions between

fluids and solids aided by the intimate pressure solution. On the other hand, the discrete dissolution of pre-existing infillings in the microstructures also explains the changing elemental compositions and the constant $^{87}\text{Sr}/^{86}\text{Sr}$ ratios of the most recent generation of infillings.

Combining the geochemical and the structural constraints

Homogeneous $^{87}\text{Sr}/^{86}\text{Sr}$ ratios of the vein and slickenside infillings characterize fluids that originated in a unique and large reservoir, most probably outside the OPA. These fluids probably invaded the contemporaneous generation of faults and microstructures formed in and around the OPA during the first regional Bresse-Rhine tectonic episode (Laurich et al. 2014) and were expelled away during the associated compressive episode along the faults and veins. However, the late flowing fluids did not carry, for instance, the necessary K for the observed illite crystallization in the gouges, as no abnormally high contents were found in the leachates of the vein and slickenside infillings. This does not mean that no K migrated into or was present in the gouges, as some of the local detrital minerals were altered during faulting and illite authigenesis was detected.

The contribution of the regional history to the geochemical scenario

The evolution of the OPA sediments is complex, as it integrates burial, uplift, continental exposure, renewed burial and two tectonic episodes, all this since deposition in a marine environment at about 175–185 Ma. Moreover, the sedimentary pile including the OPA was buried after deposition, especially during a pronounced subsidence at about 150 Ma due to basement rifting that extended widely over Europe (e.g., Nierhoff et al. 2011; Cathelineau et al. 2012, and references therein). Afterwards, gentle burial continued until about 120 Ma to a depth of about 1,350 m (Mazurek et al. 2006). A quiescent period followed until renewed uplift accompanied by erosion of the Cretaceous and Late Jurassic sediments above the OPA. From 40 to 30 Ma, subsidence resulted from a new regional rifting phase followed by a final uplift that brought the OPA back up to about 500-m depth. Sediments were deposited in the Delémont Basin during the initial Rhine-Graben rifting between 34 and 28 Ma starting with lacustrine materials called “Terre Jaune” (Pirkenseer, 2007). The associated sea transgression occurred during either the Upper Eocene (Sissingh 1998, 2006), or the Lower Oligocene (Berger et al. 2005).

In summary, the OPA was subjected to two rifting episodes interrupted by quiet episodes, then it was buried to at least 1200–1300 m and subjected to a maximum temperature of about 80–90 °C (Mazurek et al. 2006). The

tectonic–thermal episode that featured the Main Fault occurred during a Late Eocene–Early Oligocene rifting episode.

The geochemical milestones in the regional evolution

At about 175–185 Ma, seawater and living organisms were trapped within the fine-grained OPA sediments in the Jura region and nearby around. This situation initiated crystallization of calcite, often as marine biological remains, which is confirmed by homogeneous stable isotope data identical to those of plain seawater (Lerouge et al. 2014, 2015). Later, most of the initial seawater was expelled from sediments during progressive burial, while authigenic calcite crystals and biologic remnants remained within the sediments. If the homogeneous $^{87}\text{Sr}/^{86}\text{Sr}$ ratios of the advective fluids that flew along the analyzed microstructures point towards an initial voluminous reservoir, it can be assumed that this pool consisted originally of marine water. On the basis of the deposition age of the OPA and the secular variation of the seawater $^{87}\text{Sr}/^{86}\text{Sr}$ ratio (Veizer et al. 1999; McArthur et al. 2001), an $^{87}\text{Sr}/^{86}\text{Sr}$ ratio of about 0.70730 can be attributed to the seawater contemporaneous to the OPA sedimentation, while that of the flowing fluids was analytically higher as measured indirectly at 0.70774 by analysis of the microstructural infillings.

The $^{87}\text{Sr}/^{86}\text{Sr}$ value of the seawater in which the OPA sediments were deposited is within analytical uncertainty that of contemporaneous echinoderms (0.70733), while being significantly lower than that of bioclastic bivalve shells (0.70755), both analyzed by de Haller et al. (2014). Any bio-fossil of either marine or continental origin contains Sr in theoretical isotopic equilibrium with its living environment. Therefore, the $^{87}\text{Sr}/^{86}\text{Sr}$ ratios incorporated by calcite-rich precipitating fossils record the Sr signature of the water in which the fossils were living. However, the $^{87}\text{Sr}/^{86}\text{Sr}$ ratio of one of the analyzed biologic remnants from OPA matrix is above that of the probable initial seawater. It can, then, no longer be representative of its original marine environment, but rather of a later diagenetic event that could have been induced during the deepest of the burial episodes mentioned above. This changing $^{87}\text{Sr}/^{86}\text{Sr}$ ratio of bio-fossils confirms that there were interactions between pore fluids and fragile minerals known to carry and exchange easily radiogenic ^{87}Sr with their environment after initial crystallization in the ocean. This also indicates that all pore waters and minerals were affected variably by local interactions depending on the type of the waters, as well as on the temperature and, therefore, on the intensity of the recrystallizations. Even if of limited intensity, such interactions altered the initial $^{87}\text{Sr}/^{86}\text{Sr}$ ratios that rather point towards diagenetic calcite in the undeformed OPA matrix, which explains in turn the wide range of their $^{87}\text{Sr}/^{86}\text{Sr}$ ratios.

From recent regional evolution back to the origin of the initial flowing fluids

As just mentioned, the identical $^{87}\text{Sr}/^{86}\text{Sr}$ ratio for most micro-tectonic infillings suggests the occurrence of flowing fluids that originated in a large pool with an homogeneous dissolved $^{87}\text{Sr}/^{86}\text{Sr}$ ratio. Clearly, mixing of fluids or minerals having varied origins or ages cannot yield analytically identical $^{87}\text{Sr}/^{86}\text{Sr}$ ratios, as is the case here for the micro-structural infillings (Boger and Faure 1974, 1976). On the basis of the Sr isotope chronostratigraphic chart, the measured $^{87}\text{Sr}/^{86}\text{Sr}$ ratio of 0.70774 (± 0.00001) points to a potential marine reservoir of Upper-Eocene age between 38 and 36 Ma (e.g., McArthur et al. 2001; Clauer et al. 2017a).

The challenge is then in the explanation of how the $^{87}\text{Sr}/^{86}\text{Sr}$ ratio of Late-Eocene seawater (Clauer et al. 2017a) can be recorded in infillings from microstructural features generated by a tectonic–thermal event that occurred about 30 million years after the initial marine transgression, at the time of the Rhine-Graben tectonic–thermal episode. In the detail, the rifting of the Upper Rhine-Graben that occurred during the marine transgression of the Delémont Basin was mainly extensional with a strike-slip component in the Rhine-Bresse Transfer Zone (Lacombe et al. 1993). This configuration certainly favored infiltration of Late-Eocene seawater into the active contemporary faulting that developed not only major crustal faults into the basement, but also secondary faults into the nearby sediments, in and near the rock laboratory, as described by Nussbaum et al. (2011). Expectedly, seawater penetrating the fault system at that time favored precipitation of typical marine minerals, such as carbonates, sulfates and salts, as observed in faults elsewhere (e.g., Rousset et al. 2005). Precipitation of alkali-poor minerals within the rifting features from infiltrating contemporaneous seawater is the best explanation for how the initial marine $^{87}\text{Sr}/^{86}\text{Sr}$ ratio was kept identical during 30–35 million years after precipitation.

Finally, at least part of the very early veins and slickensides were re-used again during a folding/faulting event that impacted the host sediments at approximately 6.5 ± 2.5 Ma, in and around the OPA (Clauer et al. 2017b). Due to important compressions in the deeper parts of the Mont Terri anticline, some of the infillings of crustal faults from early Rhine-Graben rifting could have been solubilized again and the fluids expelled into the earlier and the newly-formed microstructures. These fluids used either paths already existing next to the major faults or new created ones that became the operating drains due to the new local stress in the Jura region. The photography of a wall from recently opening of a new gallery in the rock laboratory gives an excellent illustration of the connections between the veins of the early Rhine-Graben event

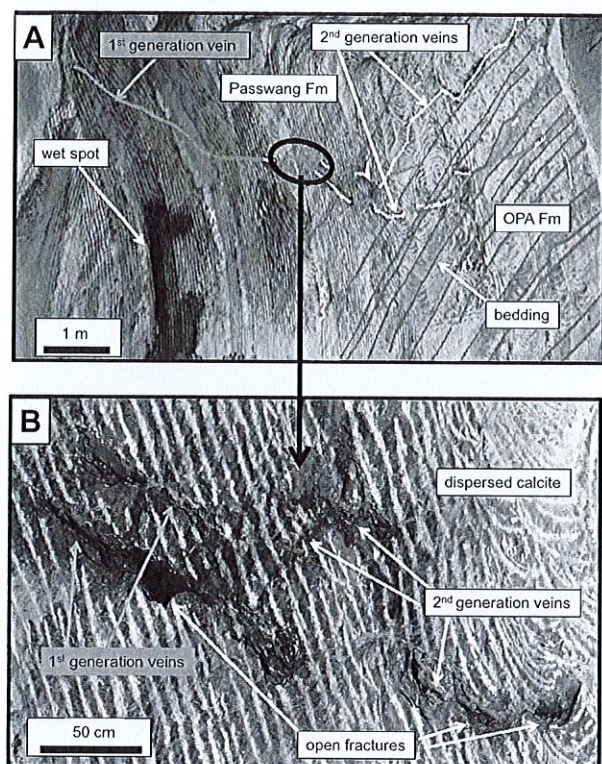


Fig. 9 **A** A picture of the wall from the new gallery of the rock laboratory showing the old and new veins, the bedding of the OPA and the stratigraphic limit between the OPA and the Passwang formations. All features are underlined by different colors. **B** The enlargement of the connection between the two generations of veins outlines also clearly open fractures

and those of the more recent Eocene episode (Fig. 9A). A magnification of the connection of these two generations of veins also highlights some open fractures (Fig. 9B). These open fractures represent perfect sinks for any flowing waters, including the present-day free waters and allow speculating that they existed during and after each tectonic–thermal activity. Therefore, it can be safely assumed that moving fluids of both tectonic–thermal episodes precipitated infillings in the created microstructures of the faulted sediments with similar to identical $^{87}\text{Sr}/^{86}\text{Sr}$ ratios and varied elemental compositions. Indeed, the “new” generation of fluids dissolved some of the initial infillings by reusing the old paths, which helped keeping the same $^{87}\text{Sr}/^{86}\text{Sr}$ ratios that they carried into the micro-features in which they combined dissolution and re-precipitation of the microstructural infillings, in and around the Main Fault. In addition, the gouges hosted mineral dissolutions and authigeneses, due to additional pressure dissolution and to organic-loaded fluids along the fault surface.

Conclusions

On the basis of previous observations and descriptions of the microstructural veins, slickensides, scaly clays and gouges from Opalinus Clay Formation in the Main Fault of the Mont Terri rock laboratory and around, the present study reports on a combined elemental and Sr isotopic investigation of soluble, mainly calcite and celestite, infillings of these microstructures. These two minerals precipitated with some elemental changes due to some interaction with the flowing fluids, but they kept an analytically identical $^{87}\text{Sr}/^{86}\text{Sr}$ ratio resulting from an isotopic heritage of infillings of micro-drains that formed during a previous tectonic–thermal event. The undeformed Opalinus Clay matrix preserved as a relict within the Main Fault contains leachable Sr with somehow varied $^{87}\text{Sr}/^{86}\text{Sr}$ ratios that are closer to those of the microstructural infillings than to those of the same rock matrix outside the Main Fault. These different $^{87}\text{Sr}/^{86}\text{Sr}$ ratios suggest that the rock volume within the fault, even not deformed, has been slightly contaminated by the fluid flows circulating in the microstructures, and diffusing also discretely into the surrounding host rocks.

The $^{87}\text{Sr}/^{86}\text{Sr}$ ratio of the infillings from microstructural veins and slickensides of the Main Fault range very narrowly at 0.70774 ± 0.00001 (2σ), suggesting that the fluid flows initiated in a large pool with an homogeneous $^{87}\text{Sr}/^{86}\text{Sr}$ ratio, like an “infinite” marine reservoir, that had also to be energetic to maintain such an isotopic homogeneity in the varied micro-features despite interactions with the wall rocks. The same $^{87}\text{Sr}/^{86}\text{Sr}$ ratio was also measured in the infillings of the same microstructures from sediments surrounding the Opalinus Clay Formation. Such homogeneous “external” seawater supply, with its specific $^{87}\text{Sr}/^{86}\text{Sr}$ ratio could occur only during the Late-Eocene period (38–36 Ma) with a Sr isotopic value agreeing with a marine incursion initiated in the western Bresse Graben and flooding over the Rhine-Bresse Graben transfer zone at that time. By assuming such a marine invasion, waters infiltrated about 30 million years later moved along the earlier created micro-tectonic veins and slickensides and leached the earlier-deposited infillings to precipitate more infillings during the late formation of the Mont Terri anticline.

On the basis of the chemical composition of the carbonated infillings from gouges, further interactions had to occur with fluids that were globally different from those responsible for the initial precipitates in the veins and the slickensides, as well as from pore waters that interacted with the dispersed calcite of the Opalinus Clay matrix around the veins. Differences in the fluids that precipitated the leachable infillings of the gouges are especially visible in the Si and Al correlations that suggest, in turn, crystallization of

illite-type crystals and dissolution of calcite and probably of other soluble mineral phases. Apparently, these fluids were reactivated during the Main Fault folding, especially in the highly deformed gouges. There, they probably interacted with minerals, which modified their elemental compositions, but not noticeably their Sr isotopic ratios. Tectonic activity was obviously the driving force for the migration/expulsion of fluids along the microstructures, intuitively occurring during the final rifting episode of the Rhine-Graben before the ultimate thin-skinned deformation that generated the Mont Terri anticline and the Main Fault.

Acknowledgements We sincerely thank Drs. B. Laurich (of the Aachen University, Germany, at the time of the study and at BGR since) and J. Urai (of the Aachen University, Germany) for supplying the microstructural samples and for the discussions during the release of the chemical data. Our thanks go also to the Mont Terri Consortium and Swisstopo for financial support of the FI research project. Dr. René Boutin, engineer of the Laboratoire d'Hydrologie et de Géochimie de Strasbourg (UdS/CNRS), deserves special thanks for the high quality of the elemental database, as well as Dr. Roy Freeman for adjusting and improving the English presentation of this publication. We also would like to give a special credit to two reviewers, who unfortunately remained anonymous, for their comments and remarks allowing an improved presentation and discussion of the results. They definitely deserve our sincere thanks.

References

- Agar SM, Prior DJ, Behrmann JH (1989) Back-scattered electron imagery of the tectonic fabrics of some fine-grained sediments: Implications for fabric nomenclature and deformation processes. *Geology* 17:901–904
- Arch J, Maltman AJ, Knipe RJ (1988) Shear-zone geometries in experimentally deformed clays: the influence of water content, strain rate and primary fabric. *J Struct Geol* 10:91–99
- Berger JP, Reichenbacher B, Becker D, Grimm M, Grimm K, Picot L, Storni A, Pirkenseer C, Schaefer A (2005) Eocene-Pliocene time scale and stratigraphy of the Upper Rhine Graben (URG) and the Swiss Molasse Basin (SMB). *Int J Earth Sci* 94:711–731
- Boger PD, Faure G (1974) Strontium-isotope stratigraphy of a Red Sea core. *Geology* 2:181–183
- Boger PD, Faure G (1976) Systematic variations of sialic and volcanic detritus in piston cores from the Red Sea. *Geochim Cosmochim Acta* 40:731–742
- Bos B, Spiers C (2001) Experimental investigation into the microstructural and mechanical evolution of phyllosilicate-bearing fault rock under conditions favouring pressure solution. *J Struct Geol* 23:1187–1202
- Bossart P, Bernier F, Birkholzer J, Bruggeman C, Connolly P, Dewonck S, Masaaki F, Herfort M, Jensen M, Matray JM, Mayor JC, Moeri A, Oyama T, Schuster K, Shigeta N, Vietor T, Wiczorek K (2017) Mont Terri rock laboratory, 20 years of research: introduction, site characteristics and overview of experiments. *Swiss J Geosci* 110:3–22
- Buatier MD, Chauvet A, Kanitpanyacharoen W, Wenk HR, Ritz JF, Jolivet M (2012) Origin and behavior of clay minerals in the Bogd fault gouge, Mongolia. *J Struct Geol* 34:77–90
- Cathelineau M, Boiron MC, Fourcade S, Ruffet G, Clauer N, Belcourt O, Coulilaly Y, Banks DA, Guillocheau F (2012) A major Late Jurassic fluid event at the basin/basement unconformity in western France: $^{40}\text{Ar}/^{39}\text{Ar}$ and K-Ar dating, fluid chemistry, and related geodynamic context. *Chem Geol* 322–323:99–120
- Clauer N, Chaudhuri S, Subramaniam R (1989) Strontium isotopes as indicators of diagenetic recrystallization scales within carbonate rocks. *Chem Geol (Isotope Geosciences)* 80:27–34
- Clauer N, Techer I, Nussbaum C, Laurich B (2017a) Geochemical signature of paleofluids in microstructures of the Main Fault in the Opalinus Clay of the Mont Terri rock laboratory, Switzerland. *Swiss J Geosci* 110:105–128
- Clauer N, Boiron MC, Nussbaum C, Techer I (2017b) Chemical clues for the extent and timing of fluid-mineral interactions in the gouge(s) from the Main Fault in the OPA. In: 35th Technical Meeting (TM-35), Porrentruy, 8–9 Feb. 2017
- de Haller A, Mazurek M, Spangenberg J, Möri A (2014) Self-sealing of faults (SF) project: Final report. Mont Terri Technical Report 2008-02, 63p
- Degeldre C, Scholtis A., Thomas B (1998) WS-A experiment: opalinus clay groundwaters and colloids. A sampling and analysis exercise at Mont Terri (June/July 1997). Analytical results. Mont Terri Project, Technical Note 97-20, 45p
- Dehandschutter B, Vandycke S, Sintubin M, Vandenberghe N, Wouters L (2005) Brittle fractures and ductile shear bands in argillaceous sediments: inferences from Oligocene Boom Clay (Belgium). *J Struct Geol* 27:1095–1112
- Doblas M (1998) Slickenside kinematic indicators. *Tectonophysics* 295:187–197
- Gay NC (1970) The formation of step structures on slickensided shear surfaces. *J Geol* 78:523–532
- Gray MB, Nickelsen RP (1989) Pedogenic slickensides, indicators of strain and deformation processes in red bed sequences of the Appalachian foreland. *Geology* 17:72–75
- Gromet LP, Dymek RF, Haskin LA, Korotev RL (1984) The North American Shale Composite: its compilation, major and trace element characteristics. *Geochim Cosmochim Acta* 48:2469–2482
- Haines SH, Kaproth B, Marone C, Saffer D, van der Pluijm B (2013) Shear zones in clay-rich fault gouge: a laboratory study of fabric development and evolution. *J Struct Geol* 51:206–225
- Holzer L, Muench B, Wegmann M, Gasser P, Flatt RJ (2006) FIB-nanotomography of particulate systems—part I: particle shape and topology of interfaces. *J Am Ceram Soc* 89:2577–2585
- Houben ME, Desbois G, Urai JL (2013) Pore morphology and distribution in the Shaly facies of Opalinus Clay (Mont Terri, Switzerland): Insights from representative 2D BIB-SEM investigations on mm to nm scale. *Appl Clay Sci* 71:82–97
- Houben ME, Desbois G, Urai JL (2014) A comparative study of representative 2D microstructures in shaly and sandy facies of Opalinus Clay (Mont Terri, Switzerland) inferred from BIB-SEM and MIP methods. *Mar Pet Geol* 49:143–161
- Ingram GM, Urai JL, Naylor MA (1997) Sealing processes and top seal assessment. In: Möller-Pedersen P, Koestler AG (eds) *Norwegian Petroleum Society Special Publications*. Elsevier, Berlin, pp 165–174
- Ishii I (2012) Microstructure and origin of faults in siliceous mudstone at the Horonobe Underground Research Laboratory site, Japan. *J Struct Geol* 34:20–29
- Jaeggi D, Laurich B, Nussbaum C, Schuster K, Connolly P (2017) Tectonic structure of the “Main Fault” in the Opalinus Clay, Mont Terri rock laboratory (Switzerland). *Swiss J Geosci* 110:67–84
- Koehn D, Passchier CW (2000) Shear sense indicators in striped bedding-veins. *J Struct Geol* 22:1141–1151
- Labat P., Maltman A.J., Bolton A., Tessier D., Ogawa Y. and Takiyawa S. (1997) Scaly fabrics in sheared clays from the decollement zone of the Barbados accretionary prism. In: Shipley TH, Ogawa Y, Blum P, Bahr JM (eds) *Proceedings of the Ocean Drilling Program, Scientific results*, vol 156, pp 59–77

- Lacombe O, Angelier J, Byrne D, Dupin JP (1993) Eocene-Oligocene tectonics and kinematics of the Rhine-Saone Continental Transform Zone (eastern France). *Tectonics* 12:874–888
- Lancelot J (ed) (2001) WS-G experiment: Geochemical pore water characterisation of reference argillaceous samples from the Mont Terri Rock Laboratory. Mont Terri Technical Note, pp 99–43
- Laurich B (2016) Evolution of microstructure and porosity in faulted Opalinus Clay. PhD thesis, RWTH-Aachen University, 2016
- Laurich B, Urai JL, Besbois G, Vollmer C, Nussbaum C (2014) Microstructural evolution of an incipient fault zone in Opalinus Clay: Insights from an optical and electron microscopic study of ion-beam polished samples from the Main Fault in the Mt-Terri Underground Research Laboratory. *J Struct Geol* 67:107–128
- Laurich B, Urai JL, Nussbaum C (2017) Microstructures and deformation mechanisms in Opalinus Clay: insights from scaly clay from the Main Fault in the Mont Terri Rock Laboratory (CH). *Solid Earth* 8:27–44
- Laurich B, Urai JL, Vollmer C, Nussbaum C (2018) Deformation mechanisms and evolution of the microstructure of gouge in the Main Fault in Opalinus Clay in the Mont Terri rock laboratory (CH). *Solid Earth* 9:1–24
- Lerouge C, Grangeon S, Claret F, Gaucher E, Blanc P, Guerrot C, Flehoc C, Wille G, Mazurek M (2014) Mineralogical and isotopic record of diagenesis from the Opalinus Clay formation at Benken, Switzerland: Implications for the modeling of pore-water chemistry in a clay formation. *Clays Clay Miner* 62:286–312
- Lerouge C, Maubec N, Wille G, Flehoc C (2015) BDB1 experiment: mineral characterization and diagenesis. Mont Terri Project, Technical Note 2014-92, p 41
- Logan JM, Dengo CA, Higgs NG, Wang ZZ (1992) Fabrics of experimental fault zones: their development and relationship to mechanical behavior. *Int Geophys Ser* 51:33–67
- Mazurek M, Hurford AJ, Leu W (2006) Unravelling the multi-stage burial history of the Swiss Molasse Basin: integration of apatite fission track, vitrinite reflectance and biomarker isomerisation analysis. *Basin Res* 18:27–50
- McArthur JM, Howarth RJ, Bailey TR (2001) Strontium isotope stratigraphy: LOWESS Version 3: Best fit to the marine Sr-isotope curve 0–509 Ma and accompanying look-up table for deriving numerical age. *J Geol* 109:155–170
- Means WD (1987) A newly recognized type of slickenside striation. *Shear Criteria Rocks* 9:585–590
- Milliken KL, Reed RM (2010) Multiple causes of diagenetic fabric anisotropy in weakly consolidated mud, Nankai accretionary prism, IODP Expedition 316. *J Struct Geol* 32:1887–1898
- Mitra G, Ismat Z (2001) Microfracturing associated with reactivated fault zones and shear zones: What it can tell us about deformation history. *Geol Soc Lond Sp Publ* 186:113–140
- Morgenstern NR, Tchalenko JS (1967) Microstructural observations on shear zones from slips in natural clays. In: *Proceedings of the Geotechnological Conference, Oslo* 1, 147–152
- Nagra (2008) Vorschlag geologischer Standortgebiete für das SMA- und das HAA-Lager, Technischer Bericht 08–04
- Nierhoff R, Clauer N, Speath G (2011) New findings on the tectono-metamorphic history of the western Rhenish Massif by K-Ar dating of metasedimentary illite. *J Geodyn* 52:129–142
- Nussbaum C, Meier O, Masset O, Badertscher N (2006) Self-sealing of fault (SF) experiment drilling of resin impregnated boreholes part of drilling campaign of phase 11 drilling data, drillcore mapping and photo documentation. Mont Terri technical note, TN 2006-22. Wabern, Switzerland: Federal Office of Topography (swisstopo)
- Nussbaum C, Bossart P (2008) Geology. In: Thury M, Bossart, P (eds) Mont Terri Rock Laboratory project, Programme 1996 to 2007 and results, Wabern, Swiss Geological Survey
- Nussbaum C, Amann F, Aubourg C, Bossart P (2011) Analysis of tectonic structures and excavation induced fractures in the Opalinus Clay, Mont Terri underground rock laboratory (Switzerland). *Swiss J Geosci* 104:187–210
- Nussbaum C, Kloppenburg A, Caër T, Bossart P (2017) Tectonic evolution around the Mont Terri rock laboratory, northwestern Swiss Jura: constraints from kinematic forward modelling. *Swiss J Geosci* 110:39–66
- Orellana LF, Violay M, Henry P, Guglielmi Y, Nussbaum C (2017) Petro-physical characterization of the Main Fault at the Mont Terri Laboratory. The 7th International Conference on Clays in Natural and Engineered Barriers for Radioactive Waste Confinement, Book of Abstracts, 268
- Paschier CW (2005) *Microtectonics*. Springer, Berlin, 366p
- Pearson FJ, Arcos D, Jordi B, Fernandez AM, Gaucher E, Pena J, Sanjuan B, Turrero J, Waber HN, Griffault L, Boisson JY, Gäbler HE, Gautschi A, Hernan P (2001) Geochemical modelling and synthesis (GM) task: Compilation of aqueous geochemistry data collected during phases 4 and 5, rock property data from all phases and results of phase 5 geochemical modelling. Mont Terri Project, Technical note 2000-36, p 161
- Pearson FJ, Arcos D, Bath D, Boisson JY, Fernández AM, Gäbler H-E, Gaucher E, Gautschi A, Griffault L, Hernán P, Waber HN (2003) Mont Terri Project – Geochemistry of Water in the Opalinus Clay Formation at the Mont Terri Rock Laboratory. Reports of the Federal Office for Water and Geology (FOWG), Geology Series No. 5, p 319
- Petit JP, Laville E (1987) Morphology and microstructures of hydroplastic slickensides in sandstone. *Geol Soc Lond Sp Publ* 29:107–121
- Pin C, Joannon S, Bosq C, Le Fèvre B, Gauthier PJ (2003) Precise determination of Rb, Sr, Ba and Pb in geological materials by isotope dilution and ICP-quadrupole mass spectrometry following selective separation of the analytes. *J Anal Spectrom* 18:135–141
- Piper DZ, Bau M (2013) Normalized rare earth elements in water, sediments, and wine: Identifying sources and environmental redox conditions. *Am J Anal Chem* 4:69–83
- Pirkenseer C (2007) Foraminifera, Ostracoda and other microfossils of the southern Upper Rhine Graben: palaeoecology, biostratigraphy, palaeogeography and geodynamic implications. PhD Thesis, University of Fribourg.
- Rieder M, Cavazzini G, D'Yyakonov YS, Frank-Kamenetskii VA, Gottardi G, Guggenheim S, Koval PV, Müller G, Neiva AMR, Radoslovich EW, Sassi FP, Takeda H, Weiss Z, Wones DR (1998) Nomenclature of the micas. *Can Mineral* 36:905–912
- Rimstidt JD (1997) Gangue mineral transport and deposition. In: Barnes HL (ed) *Geochemistry of hydrothermal ore deposits*, 3rd edn. Wiley, pp 487–515
- Roussel D, Lancelot J, Verdoux P, Clauer N, Leclerc S (2005) Influence of local fluid flow on properties of low permeability Cretaceous siltstones (South-Eastern France): Implications for a nuclear waste deep repository. *J Geochem Explor* 87:1–18
- Rutter EH, Maddock RH, Hall SH, White SH (1986) Comparative microstructures of natural and experimentally produced clay-bearing fault gouges. *Pure Appl Geophys* 124:3–30
- Saffer DM, Lockner DA, McKiernan A (2012) Effects of smectite to illite transformation on the frictional strength and sliding stability

- of intact marine mudstones: Friction and smectite transformation. *Geophys Res Lett* 39:L11304
- Samuel J, Rouault R, Besnus Y (1985) Analyse multi-élémentaire standardisée des matériaux géologiques en spectrométrie d'émission par plasma à couplage inductif. *Analyst* 13:312–317
- Sasseville C, Tremblay A, Clauer N, Liewig N (2008) K-Ar time constraints on the evolution of polydeformed fold-thrust belts: the case of the Northern Appalachians (southern Quebec). *J Geodyn* 45:99–119
- Schleicher AM, van der Pluijm BA, Solum JG, Warr LN (2006) Origin and significance of clay-coated fractures in mudrock fragments of the SAFOD borehole (Parkfield, California). *Geophys Res Lett* 33:1–5
- Sissingh W (1998) Comparative Tertiary stratigraphy of the Rhine graben, Bresse graben and Molasse basin: correlation of Alpine foreland events. *Tectonophysics* 300:249–284
- Sissingh W (2006) Syn-kinematic palaeogeographic evolution of the West European platform: correlation with Alpine plate collision and foreland deformation. *Geol Mijnbouw* 82:131–180
- Steele-Macinnis M, Manning CE (eds) (2020) Hydrothermal fluids. *Elements* 16:375–411
- Taylor SR, McLennan SM (1985) The continental crust: its composition and evolution. Blackwell, Malden
- Tjia HD (1964) Slickensides and fault movements. *Geol Soc Am Bull* 75:683–686
- Urai J, Wong SW (1994) Deformation mechanisms in experimentally deformed shales. *Ann Geophys* 12(Supplement 1):C98
- Urai JL, Humphreys FJ, Burrows SE (1980) In-situ studies of the deformation and dynamic recrystallization of rhombohedral camphor. *J Mater Sci* 15:1231–1240
- Ustaszewski K, Schmid SM (2007) Latest Pliocene to recent thick-skinned tectonics at the Upper Rhine Graben–Jura Mountains junction. *Swiss J Geosci* 100:293–312
- Ustaszewski K, Schuhmacher ME, Schmid SM (2005) Simultaneous normal faulting and extensional flexuring during rifting: an example from the southernmost Upper Rhine Graben. *Int J Earth Sci* 94:680–696
- Veizer J, Ala D, Azmy K, Bruckschen P, Buhl D, Bruhn F, Carden GAF et al (1999) $^{87}\text{Sr}/^{86}\text{Sr}$, $\delta^{13}\text{C}$ and $\delta^{18}\text{O}$ evolution of Phanerozoic seawater. *Chem Geol* 161:59–88
- Vrolijk P, van der Pluijm BA (1999) Clay gouge. *J Struct Geol* 21:1039–1048
- Warr LN, Cox S (2001) Clay mineral transformations and weakening mechanisms along the Alpine Fault, New Zealand. *Geol Soc Lond Sp Publ* 186:85–101
- Will T, Wilson CJ (1989) Experimentally produced slickenside lineations in pyrophyllitic clay. *J Struct Geol* 11:657–667

Authors and Affiliations

Norbert Clauer¹ · Isabelle Techer² · Christophe Nussbaum³

¹ Institut des Sciences de la Terre et de l'Environnement, Université de Strasbourg (UdS/CNRS), 67084 Strasbourg, France

² Equipe Associée 7352 CHROME, Université de Nîmes, 30021 Nîmes, France

³ Swiss Geological Survey, Federal Office of Topography Swisstopo, 3084 Wabern, Switzerland